International Journal of Solids and Structures 159 (2019) 171–190

Contents lists available at ScienceDirect

International Journal of Solids and Structures

journal homepage: www.elsevier.com/locate/ijsolstr

Numerical modeling of steel fiber reinforced concrete with a discrete and explicit representation of steel fibers

Luís A. G. Bitencourt Jr.[a,*], Osvaldo L. Manzoli[b], Túlio N. Bittencourt[a], Frank J. Vecchio[c]

[a] University of São Paulo, Av. Prof. Luciano Gualberto, Trav. 3 n. 380 - CEP - 05508-010 São Paulo SP, Brazil
[b] São Paulo State University - UNESP/Bauru - Av. Eng. Luiz Edmundo C. Coube 14-01 - CEP - 17033-360, Bauru SP, Brazil
[c] Department of Civil Engineering, University of Toronto, 35 St. George St., M5S 1A4, Toronto, Ontario, Canada

ARTICLE INFO

Article history:
Received 19 May 2018
Revised 20 September 2018
Available online 27 September 2018

Keywords:
Concrete
Steel fiber
Coupling finite element
Damage constitutive model
Crack propagation
Impl-Ex integration scheme

ABSTRACT

This work presents a novel numerical model based on the use of coupling finite elements to simulate the behavior of steel fiber reinforced concrete (SFRC) with a discrete and explicit representation of steel fibers. The material is described as a composite made up by three phases: concrete, discrete discontinuous fibers and fiber-matrix interface. The steel fibers are modeled using two-node finite elements (truss elements) with a one-dimensional elastoplastic constitutive model. They are positioned using an isotropic uniform random distribution, considering the wall effect of the mold. A non-rigid coupling procedure is proposed for modeling the complex nonlinear behavior of the fiber-matrix interface by adopting an appropriate constitutive damage model to describe the relation between the shear stress (adherence stress) and the relative sliding between the matrix and each fiber individually. An isotropic damage model including two independent scalar damage variables for describing the concrete behavior under tension and compression is considered. To increase the computability and robustness of the continuum damage models used to simulate matrix and interface behavior, an implicit-explicit integration scheme is used. Numerical examples involving a single fiber and a cloud of fibers are performed. Comparisons with experimental results demonstrate that the application of the numerical strategy for modeling the behavior of SFRC is highly promising and may constitute an important tool for better understanding the effects of the different aspects involved in the failure process of this material.

1. Introduction

Nowadays, it is well known that the addition of a small volume of steel fibers may increase the ductility and toughness of cementitious matrices (Bentur and Mindess, 2007). The role played by fibers is most obvious after matrix cracking has occurred, as fibers offer resistance to crack propagation. As described by Voo and Foster (2003), for plain concrete, after matrix cracking, the tensile stress immediately decreases. However, after the addition of a certain volume of steel fibers and after matrix cracking, the fibers are able to maintain a certain load bearing capacity, avoiding an abrupt failure of the composite. In addition, the crack widths are less than those of plain concrete (Deluce, 2011). Therefore, the main benefits of the addition of steel fibers in cementitious matrices are directly related to their ability to transfer stresses across cracks.

According to Bentur and Mindess (2007) this process of stress transfer depends on the internal structure of the composite and the main factors that influence the composite's behavior are (i) the structure of the bulk cementitious matrix, (ii) the shape and distribution of the fibers and (iii) the fiber-matrix interaction.

Although the application of Steel Fiber Reinforced Concrete (SFRC) has increased in the last years, being very attractive in many structures, such as tunnel linings, bridges, pavements, and pipes, there remains a lack of numerical models for simulating its behavior that consider the contribution of each component (fibers, matrix and fiber-matrix interaction) in a fully independent way.

Several approaches have also been proposed for modeling the behavior of SFRC. Continuum models for SFRC have been developed using results of structural members tested in laboratories, such as 3- and 4-point bending beams and slabs (S.K. and Ramaswamy, 2002). In some of these models, stress-strain relations are developed from the inverse analysis of the laboratory test results. These models are very limited because they are only able to reproduce the same conditions applied in the laboratory tests for specific structural members. Moreover, this type of model is highly expensive due to the large number of tests required to calibrate the model.

* Corresponding author.
E-mail address: luis.bitencourt@usp.br (L. A. G. Bitencourt Jr.).

https://doi.org/10.1016/j.ijsolstr.2018.09.028
0020-7683/

As an alternative approach, various analytical models (Lee et al., 2012; 2011; Rolf et al., 2013; Zhan and Meschke, 2014) were also proposed and implemented in computational programs. An interesting model called Diverse Embedment Model (DEM) (Lee et al., 2011) has been recently developed in order to describe the tension behavior of SFRC. The DEM considers the effects of the fiber geometry, the fibers' distribution and orientation, characteristics of the single pullout response and the influence of the structural member dimensions.

Models based on mixture theory have also been developed (Manzoli et al., 2008; Mora et al., 2011; Vrech et al., 2016). In these models, the composite stresses are obtained by summing the stresses of each constituent, which are weighted according to their corresponding volumetric participation. Manzoli et al. (2008) and Mora et al. (2011) use a Continuum Strong Discontinuous Approach (CSDA) for modeling the failure behavior of the composite, while in the model proposed by Vrech et al. (2016), a continuum (smeared crack) formulation, based on the microplane theory is applied.

Recently, various studies have focused on the development of models that include a discrete treatment of fibers. An explicit representation is adopted in some models (Pros et al., 2012; Cunha et al., 2011; 2012; Fang and Zhang, 2013; Kang and Bolander, 2015), whereas in other models, only interaction forces are considered to account for the presence of the fibers (Radtke et al., 2010; 2011; Etse et al., 2012; Caggiano et al., 2012). This type of approach is appealing because the mechanical response of this material is highly dependent on both the distribution of the steel fibers and the interaction of each fiber with the cementitious matrix. In addition, these models are very useful for considering factors, such as the casting procedure, vibrations and wall effects introduced by the formwork (Švec et al., 2014). Covering all these cases using only experimental investigations would be very expensive. Hence, a numerical model with a discrete treatment of the fibers seems to be a natural way to simulate the failure behavior of this material.

In discrete models based on the finite element method with an explicit representation of the fibers, non-matching meshes are often considered between the cloud of steel fibers and cementitious matrix (i.e., the meshes of the cementitious matrix and fiber cloud are generated in a completely independent way). Then, a coupling procedure is applied to couple these independent overlapping meshes. Usually, a rigid coupling (perfect adherence) is applied and the fiber-matrix interaction is included in the constitutive model (stress x strain relation) adopted to describe the behavior of the fibers (Pros et al., 2012; Cunha et al., 2011; 2012). In turn, this relation is obtained through analytical expressions deduced from pullout tests, as for example, the expressions proposed by Laranjeira (2010) which are deduced from pullout tests carried out by Laranjeira et al. (2010a,b). In Radtke et al. (2011), the nonlinear behavior of the fiber-matrix interaction is described by the model proposed by Hartig et al. (2008).

In the literature, many numerical models have been proposed for modeling the failure process of SFRC based on the continuous and discontinuous approaches. In the model proposed by Radtke et al. (2011), the matrix behavior is described by an isotropic damage model with an exponential softening law. This damage model is equipped with a simple regularized fracture energy model (details can be found in Bazănt and Oh (1983)) and with the gradient-enhanced damage model proposed by Peerlings et al. (1996) to avoid the mesh dependence. Damage models with similar approaches were also employed in the researches developed by Radtke et al. (2010) and Pros et al. (2012). A heuristic crack model with joint elements is adopted by Parés (2011). In Etse et al. (2012), the failure behavior of SFRC is evaluated at both the macro and mesoscale levels of observation. These authors employ a discrete crack formulation based on the use of zero-thickness interface elements proposed by Carol et al. (1997) for plain concrete. A failure criterion defined in terms of the normal and shear stress components acting on the joint plane is adopted. For the pre-peak regime, a linear elastic model is considered, while the post-peak is formulated in terms of the fracture energy release under failure modes I and/or II. Analytical expressions proposed by Soroushian and Lee (1990) are employed to define the number of crossing fibers per interface and the respective orientation factor. In the model proposed by Zhan and Meschke (2016), the failure process of SFRC is described using finite elements with high aspect ratio developed by Manzoli et al. (2012).

A few 3D numerical models are available in literature for modeling SFRC. Parés (2011) proposes a 3D extension of the formulation developed by Pros et al. (2012). However, for all the numerical examples performed, the failure pattern exhibits only one crack and to define the constitutive model for each fiber, the angle between the fiber and the failure pattern must be known beforehand. For the 3D model proposed Cunha (2010), only experiments with a previously defined fracture plane have been analyzed.

As an alternative to standard finite element formulations, Radtke et al. (2011) propose a model based on Partition of Unity Finite Element Method (PUFEM). Thus, the presence of discrete fibers is considered employing the partition of unity property of finite element shape functions, without explicitly meshing them to ensure numerical efficiency. Lattice models have also been developed as an alternative for modeling fiber reinforced cement composites. In the model proposed by Kang et al. (2014), fibers can be positioned freely in the computational domain, irrespective of the background lattice representing the matrix phase.

This paper proposes a new approach for modeling the failure processes of SFRC with a discrete and explicit representation of steel fibers. The material is described as a composite made up by three phases: concrete, discrete discontinuous fibers and fiber-matrix interface. A special coupling finite element developed by Bitencourt Jr. et al. (2015) is employed to couple the independent overlapping meshes of the matrix (2D or 3D solid elements) and a cloud of steel fibers. Two-node finite elements and elastoplastic constitutive model are used for modeling the steel fibers. The fibers are generated and positioned randomly using an isotropic uniform random distribution, taking into account the wall-effect of the mold. The complex nonlinear behavior of the interaction between concrete and fibers is modeled through a damage constitutive model and the non-rigid coupling procedure proposed by Bitencourt Jr. et al. (2015). An isotropic damage model with two independent scalar damage variables proposed by Cervera et al. (1996) is used to describe the behavior of the concrete. In addition, an implicit-explicit integration scheme is employed to increase the robustness of the constitutive models and to accelerate the nonlinear convergence. Recently, this approach has been applied as an alternative methodology to represent rebars and their bond-slip behavior against concrete (Bitencourt Jr. et al., 2018).

The remainder of this paper is organized as follows. The strategy employed to represent steel fibers with a discrete and explicit representation is presented in Section 2. Section 3 presents the continuum damage model and the implicit-explicit integration scheme used to represent the concrete behavior. In Section 4 three numerical analyses are conducted in order to validate the proposed approach. Finally, a summary and the main conclusions are presented in Section 5.

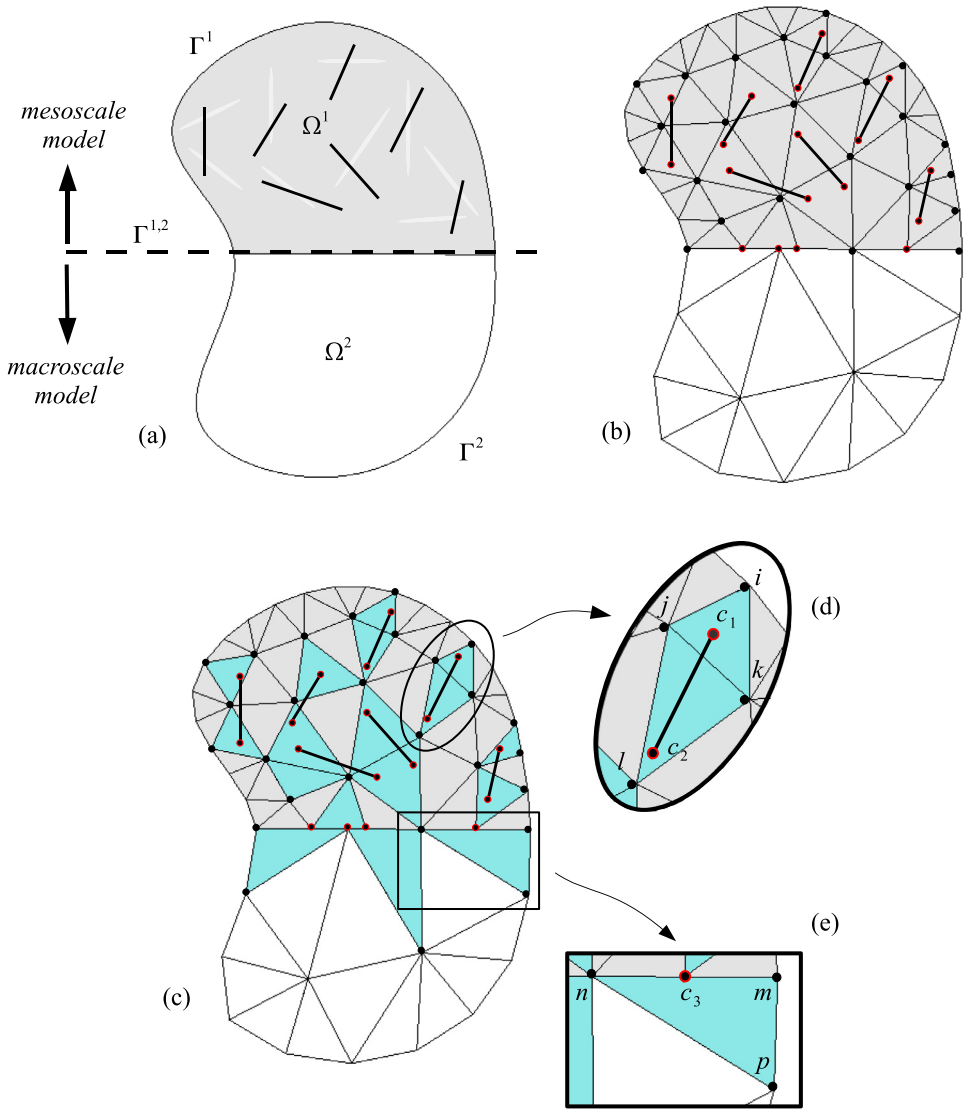

Fig. 1. Coupling procedure for non-matching finite element meshes: (a) definition of the problem; (b) process of identification of the nodes that will compose the CFEs; (c) creation and insertion of the CFEs; (d) detail of coupling in overlapping meshes; and (e) detail of coupling in non-overlapping meshes.

2. Numerical model for steel fiber reinforced concrete

2.1. Discrete and explicit representation of steel fibers

The numerical model proposed for steel fiber reinforced concrete with a discrete and explicit representation of steel fibers is based on the use of Coupling Finite Elements (CFEs) developed by Bitencourt Jr. et al. (2015).

Fig. 1 illustrates the most general case, i.e., when a concurrent multiscale model is adopted. In this problem, the coupling technique is employed to couple both the interface between the subdomains Ω^1 (mesoscale) and Ω^2 (macroscale), defined by $\Gamma^{1,2} = \Gamma^1 \cap \Gamma^2$ (non-overlapping meshes), and to describe the interaction between concrete and steel fibers of the region discretized in mesoscale (overlapping meshes). As the focus of this paper is to present how to consider the presence of fibers individually, the aggregates are not explicitly represented.

The strategy proposed can be summarized as follows:

1. Discretization of the macroscale and mesoscale regions based on the geometry of the structural member (Fig. 1(b));
2. Identification of the loose nodes at the common boundary interface of the subdomains and in the region where a mesoscale approach is adopted (here represented by the red nodes in Fig. 1(b));
3. Definition and insertion of CFEs to couple the subdomains and to describe the interaction between concrete and fibers (Fig. 1(c)).
4. Assembly of the CFEs in the system of equations of the problem, according to the law that describes the interaction between the independent meshes.

According to Bitencourt Jr. et al. (2015), each CFE has the same nodes of an underlying finite element of the existing mesh and an extra node, coinciding with the loose node (herein designated coupling node) that belongs to its domain. As a consequence, the CFEs overlap the finite elements of the original mesh containing the coupling nodes.

Fig. 1(d) shows an example of coupling between overlapping meshes, where two coupling finite elements $CFE_1 = \{i, j, k, c_1\}$ and $CFE_2 = \{j, l, k, c_2\}$ were used, whose nodes c_1, and c_2, respectively are their coupling nodes. At the common boundary interface, to each loose node, a coupling finite element is also inserted to connect the non-overlapping meshes, using as base an existing finite element, which has one face (for 3-node triangles defined

Table 1
Pseudo code of the algorithm developed for generating steel fibers.

```
Read input data
Calculate N_f
for n = 1 : N_f
    Calculate the C.G. of i^th fiber X̄ = (x̄_i, ȳ_i, z̄_i)
        Check if the C.G. is valid
    Calculate the coordinates of the i^th fiber end-nodes X̄^e = (x_i^e, y_i^e, z_i^e)
        Check if the end-node coordinates are valid
end for
Save output file
```

by two nodes) along at the common boundary interface. An example is shown in Fig. 1(e), where the coupling finite element $CFE_3 = \{m, n, p, c_3\}$ is introduced, with c_3 being the coupling node. Note that for each loose node, one coupling finite element is required.

The CFEs share nodes with both non-matching meshes and are used to ensure the compatibility of displacements and to transfer interaction forces between non-matching meshes. The interaction forces between the non-matching meshes may also be described by an appropriate constitutive model applied in the CFEs. This is one of the major advantages of the technique, since a rigid (full compatibility of displacements) or non-rigid (degrading interface) coupling can be considered easily. Thus, the use of this technique for modeling reinforced composite is very appealing, since reinforcement, matrix and reinforcement-matrix interface can be modeled independently.

Fig. 1(c) illustrates the final configuration of the mesh, with all the CFEs. After the application of the coupling procedure, the global internal force vector and the stiffness matrix can be written as:

$$\mathbf{F}^{int} = \underbrace{A_{e=1}^{nel_C}(\mathbf{F}_e^{int})_C}_{\text{concrete elements}} + \underbrace{A_{e=1}^{nel_{SF}}(\mathbf{F}_e^{int})_{SF}}_{\text{steel fibers}} + \underbrace{A_{e=1}^{nel_{CFE}}(\mathbf{F}_e^{int})_{CFE}}_{\text{coupling elements}} \tag{1}$$

$$\mathbf{K} = \underbrace{A_{e=1}^{nel_C}(\mathbf{K}_e)_C}_{\text{concrete elements}} + \underbrace{A_{e=1}^{nel_{SF}}(\mathbf{K}_e)_{SF}}_{\text{steel fibers}} + \underbrace{A_{e=1}^{nel_{CFE}}(\mathbf{K}_e)_{CFE}}_{\text{coupling elements}} \tag{2}$$

where A stands for the finite element assembly operator, the first and second terms of Eqs. 1 and 2 are related to the finite elements employed to represent the concrete and steel fibers, respectively, and the third term is tied to the introduction of the CFEs. Note that the coupling procedure does not introduce any additional degree of freedom in the global problem and can be regarded as a preprocessing stage.

2.2. Fiber distribution and orientation in concrete

From the fiber content and the geometrical properties of both the steel fiber and concrete specimen, a cloud of fibers is generated using an isotropic uniform random distribution, according to the algorithm proposed by Cunha (2010). Steel fibers are represented by straight lines for both straight and hooked fibers with a null thickness. It is also worth to mention that the use of straight lines for hooked fibers is feasible, since in this work the effect of the end-hooked is considered in the bond-slip law adopted to describe the fiber-matrix interaction.

Table 1 summarizes the algorithm developed in the form of pseudo code. The first step comprises the initialization of variables to be used for generating the desired cloud of fibers (read input data). Based on these data, the number of steel fiber to be generated is calculated, which will define the number of loops necessary for generating fiber by fiber, each position and orientation inside specimen's domain. When at least one of the fiber end-nodes violates the boundary conditions, a new fiber orientation is generated up to a predefined number of attempts. With this procedure,

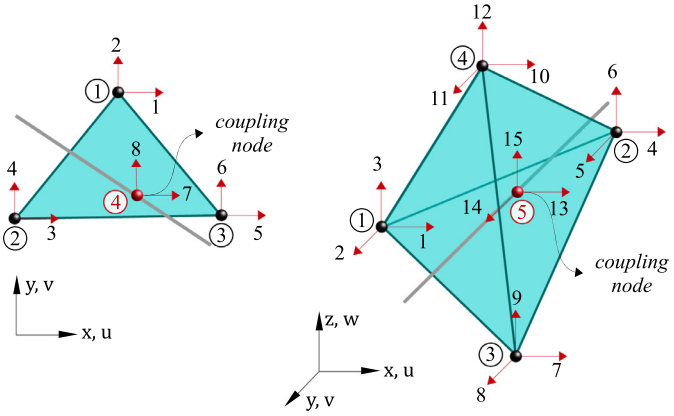

Fig. 2. 2D and 3D CFEs based on linear interpolation functions for displacements: 3-noded triangular element with the C_{node} and 4-noded tetrahedral element with the C_{node}.

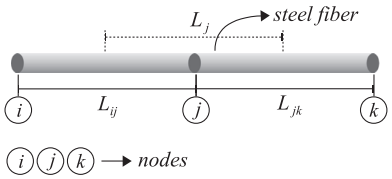

Fig. 3. Influence length of the coupling node.

a fiber alignment near the boundary surfaces is obtained, taking into account the wall effect of the mold. Finally, after a number of loops equal to N_f is achieved, the fibers end-node coordinates are saved into an output file, to be further imported by the preprocessor program.

Due to the high computational cost of 3D analyses, many analyses in this work are performed in 2D. In these cases, after the generation of a cloud of fiber in 3D, the third components of the Cartesian axis are suppressed to account only the projection of each fiber length on the plane of analysis.

2.3. Coupling scheme for non-matching meshes

The scheme proposed by Bitencourt Jr. et al. (2015) to couple non-matching meshes is applied in this work to couple overlapping non-matching meshes of the concrete and a cloud of fibers. Thus, concrete-steel fiber interaction is described by the use of CFEs. To understand the interaction force introduced by these elements, let us consider a standard isoparametric finite element of domain Ω^e, with number of nodes equal to nn, and shape functions $\overline{N}_i(\mathbf{X})(i = 1, nn)$, which are defined for the material points $\mathbf{X} \in \Omega^e$, such that the displacement $\overline{\mathbf{U}}$ at any point in its domain can be approximated in terms of its nodal displacements $\mathbf{D}_i$ $(i = 1, nn)$, as follows:

$$\overline{\mathbf{U}}(\mathbf{X}) = \sum_{i=1}^{nn} \overline{N}_i(\mathbf{X})\mathbf{D}_i. \tag{3}$$

As defined by Bitencourt Jr. et al. (2015), the CFE is a finite element which has the above described nodes of the standard isoparametric finite element as well as an additional node, $nn + 1$, called coupling node (C_{node}), situated at the material point $\mathbf{X}_c \in \Omega^e$, as illustrated in Fig. 2. In this figure, the additional node is the loose node of the bar that belongs to the domain of its respective element of concrete. For these cases, the C_{node} are the fourth and fifth node of the triangular and tetrahedral coupling finite elements, respectively, as shown in Fig. 2.

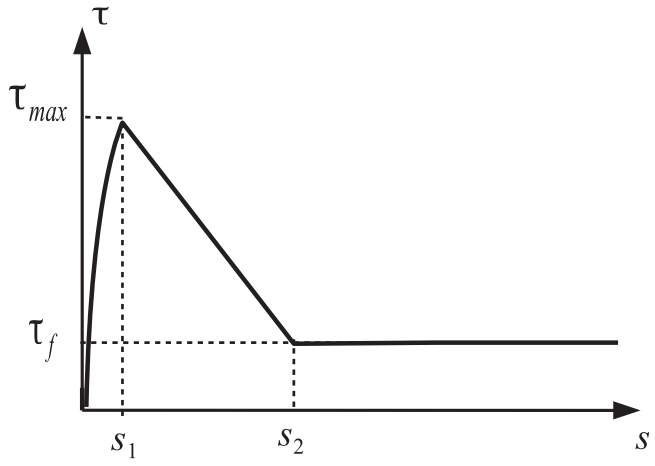

Fig. 4. Bond-slip relation adopted to described the fiber-matrix interaction.

The relative displacement, $[[\boldsymbol{U}]]$, defined as the difference between the displacement of the C_{node} and the displacement of the material point $\mathbf{X}_c$, can be evaluated using the shape functions of the underlying finite element, $\overline{N}_i(\mathbf{X}_c)(i = 1, nn)$, as follows:

$$[\![\mathbf{U}]\!] = \mathbf{D}_{nn+1} - \overline{\mathbf{U}}(\mathbf{X}_c) = \mathbf{D}_{nn+1} - \sum_{i=1}^{nn} \overline{N}_i(\mathbf{X}_c)\mathbf{D}_i = \mathbf{B}_e\mathbf{D_e}, \tag{4}$$

where the matrix $\mathbf{B}_e = [-\overline{\mathbf{N}}_1(\mathbf{X}_c) \;\; -\overline{\mathbf{N}}_2(\mathbf{X}_c) \;\; \ldots \;\; -\overline{\mathbf{N}}_{nn}(\mathbf{X}_c) \;\; \mathbf{I}]$, $\overline{\mathbf{N}}_i = \overline{N}_i\mathbf{I}$, $\mathbf{I}$ is the identity matrix of order 2 or 3, for 2D and 3D problems, respectively, and $\mathbf{D}_e = \left\{\mathbf{D}_1 \;\; \mathbf{D}_2 \;\; \cdots \;\; \mathbf{D}_{nn+1}\right\}^T$ stores the displacement components of the CFE.

Thus, the internal virtual work of the CFE is given by

$$\delta W_e^{int} = \delta[\![\mathbf{U}]\!]^T\mathbf{F}([\![\mathbf{U}]\!]), \tag{5}$$

where $\mathbf{F}([[\boldsymbol{U}]])$ is the reaction force owing to the relative displacement $[[\boldsymbol{U}]]$ and $\delta[[\mathbf{U}]]$ is an arbitrary virtual relative displacement, compatible with the boundary conditions of the problem. Using the same approximation for the virtual relative displacement as that used for the relative displacement given by Eq. 4, i.e., $\delta[\![\mathbf{U}]\!] = \mathbf{B}_e\delta\mathbf{D}_e$, the internal force vector of the coupling finite element can be expressed as follows:

$$\mathbf{F}_e^{int} = \mathbf{B}_e^T\mathbf{F}([\![\mathbf{U}]\!]). \tag{6}$$

Accordingly, the corresponding tangent stiffness matrix of the CFE can be obtained by the following expression:

$$\mathbf{K}_e = \frac{\partial\mathbf{F}_e^{int}}{\partial\mathbf{D}_e} = \mathbf{B}_e^T\mathbf{C}_{tg}\mathbf{B}_e \tag{7}$$

where $\mathbf{C}_{tg} = \partial\mathbf{F}([\![\mathbf{U}]\!])/\partial[\![\mathbf{U}]\!]$ is the tangent operator of the constitutive relation between reaction force and the relative displacement.

2.3.1. Perfect adherence

The perfect adherence between concrete and steel fibers is considered by adopting the rigid coupling scheme proposed by Bitencourt Jr. et al. (2015). Thus, the displacement compatibility of the two non-matching meshes is described by the linear elastic relation between the reaction force and the relative displacement given by the Eq. 8, by assuming a high elastic stiffness value for the components $\tilde{C}$ in the matrix of elastic constants $\mathbf{C}$ (Eq. 9).

$$\mathbf{F} = \mathbf{C}[\![\mathbf{U}]\!] = \mathbf{CB_eD}_e \tag{8}$$

$$\mathbf{C} = \begin{bmatrix} \tilde{C} & 0 & 0 \\ 0 & \tilde{C} & 0 \\ 0 & 0 & \tilde{C} \end{bmatrix} \tag{9}$$

It is important to note that, $\tilde{C}$ plays the role of a penalty variable on the relative displacement, and because of the equilibrium conditions, the interaction force $\mathbf{F}$ in Eq. 8 must be bounded. Hence, when the elastic constants tend towards a very high value, the relative displacement components $[[\boldsymbol{U}]]$ must tend to zero.

2.3.2. Loss of adherence

The non-rigid version of the coupling scheme proposed by Bitencourt Jr. et al. (2015) that allows a relative displacement between concrete and steel fibers is used to represent the loss of adherence.

For this type of application, a local coordinate system, (**n, s, t**), oriented such that the axis **n** coincides with the fiber axial orientation is necessary to describe movement (sliding) of the fiber with respect to the concrete matrix in the direction of the fiber axis. Thus, the relative displacement and its corresponding reaction force can be expressed as $[[\mathbf{u}]] = \mathbf{R}[[\mathbf{U}]]$ and $\mathbf{f} = \mathbf{RF}$, respectively, where $\mathbf{R}$ is the orthogonal rotation matrix between the local and global reference systems.

In general, these models are described by a relationship between the local (shear) stress, τ, acting at the reinforcement-matrix interface, and the relative displacement (interface slip), s.

Since the CFE introduces into the problem an interaction force between the concrete matrix and the fiber, at the coupling node, one may consider that this force results from the bond (shear) stress, τ, on the bond area (concrete-fiber interface) in the vicinity of the coupling node. Therefore, by assuming that the bond (shear) stress is constant in the vicinity of the node and that the size of the vicinity (influence length) that contributes to the resultant force in a specific node corresponds to the average of the distances between the node ''j'' and its adjacent nodes of the fiber ''i'' e ''k'', as shown in Fig. 3, the interaction force may be expressed as:

$$f_{n_j} = \tau([\![u_{n_j}]\!])PL_j, \tag{10}$$

where $L_j = (L_{ij} + L_{jk})/2$ is the influence length and P is the perimeter of the fiber cross-section. Note that the slip, s, is given by the relative displacement in direction n, i.e., $s = [\![u_n]\!]$. Since the shear stresses act in the longitudinal direction of the fiber, they only contribute to the component of the force in the direction n. The remaining transverse components of the resultant force can be expressed as:

$$f_{s_j} = \tilde{c}[\![u_{s_j}]\!]PL_j \tag{11}$$

and

$$f_{t_j} = \tilde{c}[\![u_{t_j}]\!]PL_j. \tag{12}$$

adopting a high value between 10^6 to 10^9 (MPa/mm) for the elastic constant $\tilde{c}$, as suggested by Bitencourt Jr. et al. (2015).

Loss of adherence model might be easily represented by assuming an elastic constitutive model adopting $\tau([\![u_{n_j}]\!]) = c_n[\![u_{n_j}]\!]$ in the Eq. 10.

2.3.3. A Continuum damage model to describe bond slip

For loss of adherence, a constitutive model based on the continuum damage theory is used to describe the constitutive relationship between the shear stress (adherence stress) and the relative sliding. The main components of this model are listed in Table 2, where c_n is the elastic stiffness constant (unit of stress per unit of length), $d \in [0, 1]$ is the scalar damage variable, $\overline{\tau}$ is the effective shear stress, and r is the strain-like internal variable that assumes the maximum value reached by $|\overline{\tau}|$ during the load process. The function $q(r)$ represents the hardening/softening law of the constitutive model, and it may be adjusted to fit any bond-slip model of type $\tau(s)$, considering the relationship $q(r) = \tau(r/c_n)$.

Taking as an example a bond slip model constructed based on the description given by Cunha (2010) for the pullout response of

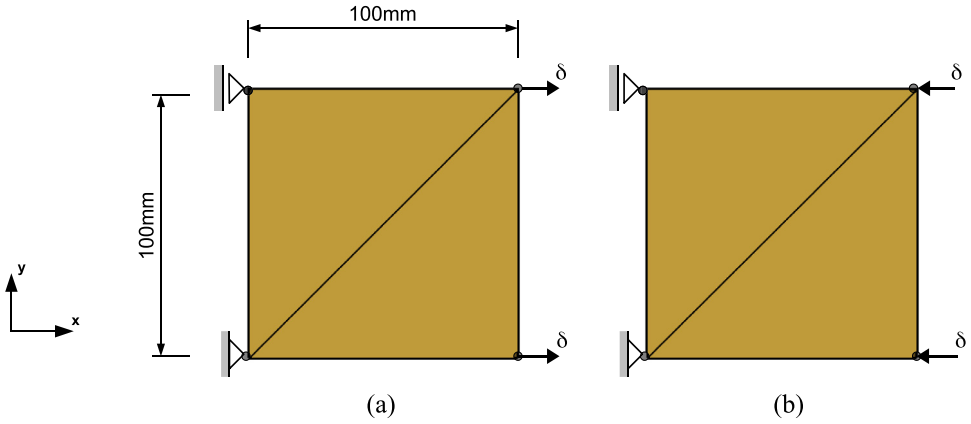

Fig. 5. Uniaxial test setup: (a) tension and (b) compression load.

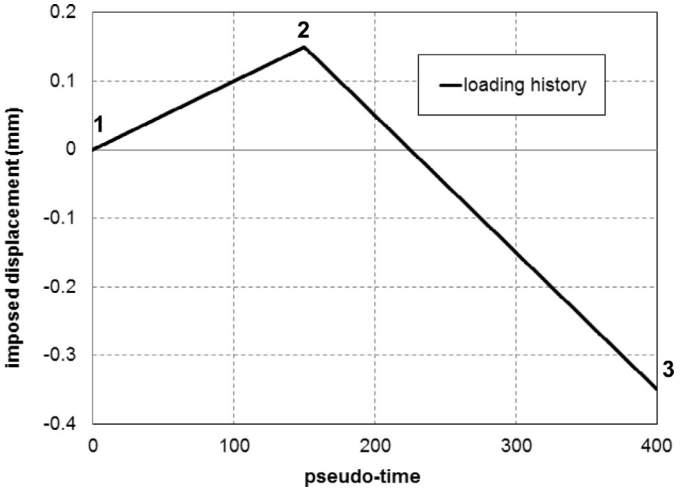

Fig. 6. Loading history considered in the uniaxial test.

Table 2
Components of the continuum damage model to describe bond slip.

constitutive relation	$\tau = (1-d)\overline{\tau}$
effective shear stress	$\overline{\tau} = c_n[[u_n]]$
damage criterion	$\phi = \|\overline{\tau}_b\| - r \le 0$
evolution law of the internal variable	$r = max[\|\overline{\tau}\|]$
damage evolution	$d(r) = 1 - \frac{q(r)}{r}$

hooked steel fibers, the fiber-matrix interaction is described by the relation depicted in Fig. 4 and given by the following equations:

$$\tau(s) = \begin{cases} \tau_{max}\left(\frac{s}{s_1}\right)^{\alpha} & \text{if} \quad s \le s_1 \\ \tau_{max} - \frac{(\tau_{max}-\tau_f)(s-s_1)}{s_2-s_1} & \text{if} \quad s_1 \le s \le s_2 \\ \tau_f & \text{if} \quad s > s_2 \end{cases}, \tag{13}$$

and the corresponding hardening/softening law is defined in terms of the stress- and strain-like internal variable as:

$$q(r) = \begin{cases} \tau_{max}\left(\frac{r/c_n}{s_1}\right)^{\alpha} & \text{se} \quad 0 \le r/c_n \le s_1 \\ \tau_{max} - \frac{(\tau_{max}-\tau_f)(r/c_n-s_1)}{s_2-s_1} & \text{se} \quad s_1 \le r/c_n \le s_2 \\ \tau_f & \text{se} \quad r/c_n > s_2 \end{cases} \tag{14}$$

2.3.4. Implicit-explicit integration scheme for the continuum damage model to describe bond-slip

The Impl-Ex integration scheme proposed by Oliver et al. (2006, 2008) is used for the integration of the damage constitutive model developed to describe the bond-slip behavior between concrete and fiber. The integration algorithm is summarized in Table 3. As the constitutive model corresponds to a discrete relation, the integration is performed in a closed-form, such that, given the relative displacement $[\![u_{n_{n+1}}]\!]$ in the direction of the fiber axis, at pseudo time t_{n+1}, a shear stress $\tilde{\tau}_{n+1}$ is evaluated explicitly, to be used to fulfill the balance equation and to compute the algorithmic tangent operator. Note that the strain-like internal variable increment (Δr_{n+1}) evaluated at pseudo-time step t_{n+1} (see step (iii) in Table 3) is used in the next pseudo-time step to evaluate the strain-like internal variable explicitly $(\tilde{r}_{n+1})$.

3. Concrete modeling

To describe the nonlinear behavior of concrete using a continuous approach, the rate-independent version of the constitutive model based on Continuum Damage Mechanics Theory (CDMT) proposed by Cervera et al. (1996) was employed. This constitutive model was implemented in this research using a special implicit-explicit integration scheme to increase its robustness and accelerate the convergence during the nonlinear analysis. The main ingredients and features of this constitutive model are described in the following.

3.1. A continuum isotropic damage model with distinct tensile and compressive responses

This constitutive model is able to describe distinct responses when submitted to tension or compression. To do this, its components such as damage variable, damage criterion, equivalent stress and damage evolution rule are defined separately, with the aid of the indices $(+)$ and $(-)$, for tension and compression, respectively.

The effective stress tensor assumes the form

$$\bar{\boldsymbol{\sigma}} = \mathbb{C} : \boldsymbol{\varepsilon}, \tag{15}$$

where $\mathbb{C}$ is the fourth order linear-elastic constitutive tensor, and $\boldsymbol{\varepsilon}$ is the second order strain tensor. Then, in order to differentiate clearly the contribution due to tension $\left(\bar{\boldsymbol{\sigma}}^{+}\right)$ and compression $\left(\bar{\boldsymbol{\sigma}}^{-}\right)$, the effective stress tensor is split as follows:

$$\bar{\boldsymbol{\sigma}}^{+} = \langle\bar{\boldsymbol{\sigma}}\rangle = \sum_{i=1}^{3} \langle\bar{\sigma}_i\rangle \boldsymbol{p}_i \otimes \boldsymbol{p}_i \tag{16}$$

and

$$\bar{\boldsymbol{\sigma}}^{-} = \bar{\boldsymbol{\sigma}} - \bar{\boldsymbol{\sigma}}^{+}, \tag{17}$$

where $\bar{\sigma}_i$ denotes the ith principal stress value from tensor $\bar{\boldsymbol{\sigma}}$, and $\boldsymbol{p}_i$ represents the unit vector associated with its respective principal direction. The symbols $\langle\cdot\rangle$ are the Macaulay brackets, giving

Table 3
Impl-Ex integration scheme for the continuum damage model to describe bond-slip.

INPUT: $[\![u_{n_{n+1}}]\!]$, r_n, Δr_n
(i) Compute the effective stress
$\overline{\tau}_{n+1} = c_n [\![u_{n_{n+1}}]\!]$
(ii) Check loading/unloading conditions
if $\|\overline{\tau}_{n+1}\| \leq r_n$, then
update damage threshold: $r_{n+1} = r_n$
else
update damage threshold: $r_{n+1} = \|\overline{\tau}_{n+1}\|$
(iii) Compute the strain-like internal variable increment
$\Delta r_{n+1} = r_{n+1} - r_n$
(iv) Compute explicit linear extrapolation of the strain-like internal variable
$\tilde{r}_{n+1} = r_n + \frac{\Delta r_n}{\Delta t_n}\Delta t_{n+1}$; $\Delta t_{n+1} = t_{n+1} - t_n$ and $\Delta t_n = t_n - t_{n-1}$
(v) Update the damage parameters
$\tilde{d}_{n+1}(\tilde{r}_{n+1}) = 1 - \frac{\tilde{q}_{n+1}(\tilde{r}_{n+1})}{\tilde{r}_{n+1}}$
(vi) Compute the shear stress
$\tilde{\tau}_{n+1} = (1 - \tilde{d}_{n+1})\overline{\tau}$
OUTPUT: $\tilde{\tau}_{n+1}$, r_{n+1}, Δr_{n+1}
Compute the effective algorithmic tangent operator
$\tilde{c}^{\tan}_{n_{n+1}} = \frac{\partial \tilde{\tau}_{n+1}}{\partial [\![u_{n_{n+1}}]\!]} = (1 - \tilde{d}_{n+1})c_n$

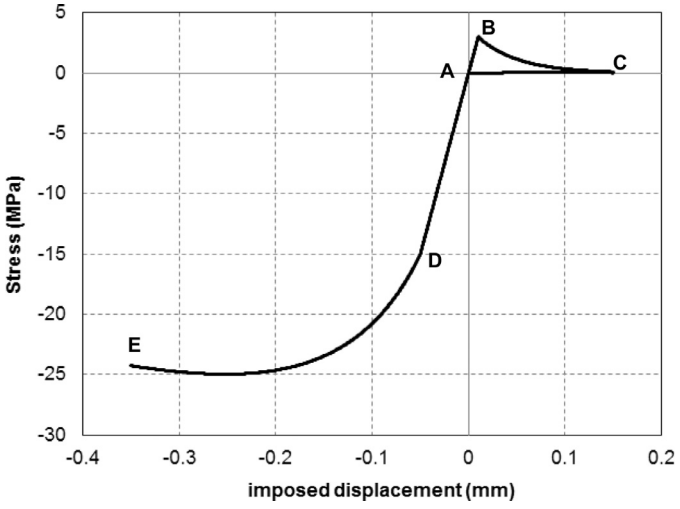

Fig. 7. Horizontal stress x imposed displacement.

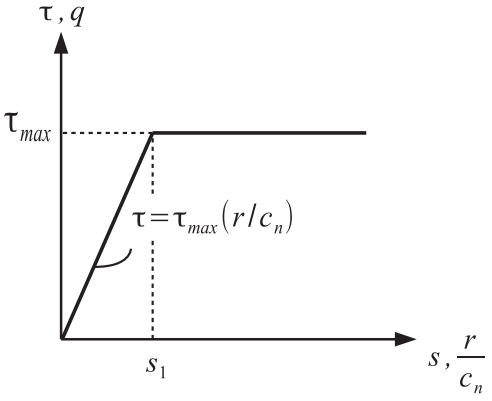

Fig. 9. Fiber-matrix interface model employed.

the value of the enclosed expression when positive, and setting a zero value if negative.

To define the concepts of loading, unloading and reloading conditions for general stress states, two positive scalar variables are introduced, termed equivalent effective tensile and compression norms, defined in this work by the expressions:

$$\tilde{\boldsymbol{\tau}}^{+} = \sqrt{\tilde{\boldsymbol{\sigma}}^{+} : \boldsymbol{C}^{-1} : \tilde{\boldsymbol{\sigma}}^{+}}, \tag{18}$$

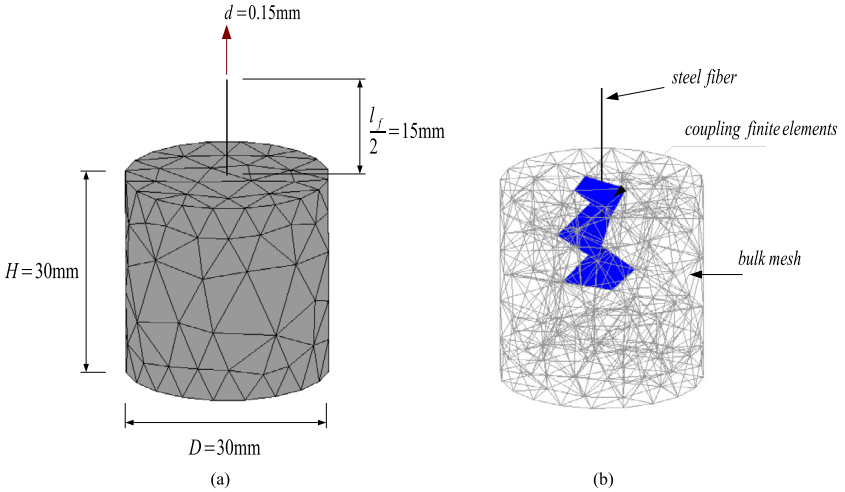

Fig. 8. 3D numerical model of the pullout test of single straight fiber embedded on one side: (a) setup of the pullout tests, and (b) detail of the coupling procedure.

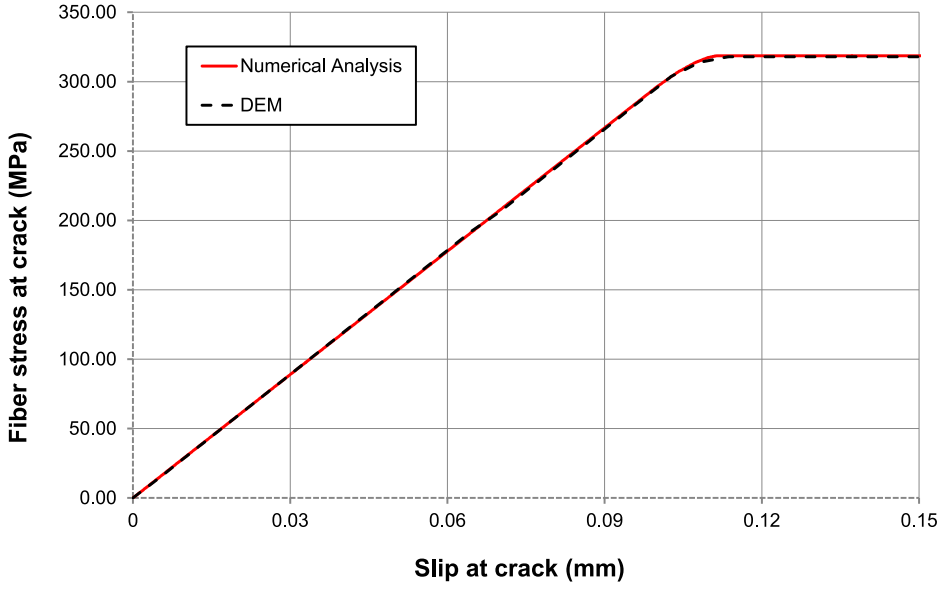

Fig. 10. Fiber stress at crack with $l_a = 0.5l_f$ for straight fiber.

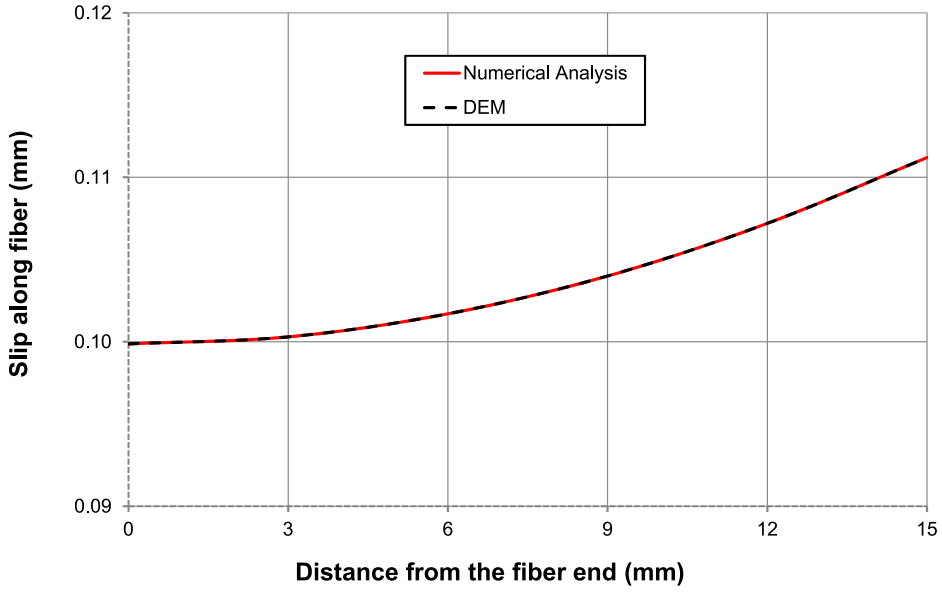

Fig. 11. Variation of the slip along the fiber when end slip is 0.1mm.

and

$$\bar{\tau}^{-} = \sqrt{\sqrt{3}\left(K\bar{\sigma}^{-}_{oct} + \bar{\tau}^{-}_{oct}\right)}. \tag{19}$$

where $K = \sqrt{2}(\beta - 1)/(2\beta - 1)$ is a material property, which depends on the ratio between the biaxial and uniaxial compressive strengths of the concrete, β. According to Cervera et al. (1996), typical values for concrete are $\beta = 1.16$ and $K = 0.171$. In Eq. 19, $\bar{\sigma}^{-}_{oct}$ and $\bar{\tau}^{-}_{oct}$ are the octahedral normal and shear stresses, respectively, obtained from $\bar{\sigma}^{-}$, and can be written as:

$$\bar{\sigma}^{-}_{oct} = \frac{1}{3}I_1, \tag{20}$$

and

$$\bar{\tau}^{-}_{oct} = \sqrt{\frac{2J_2}{3}}, \tag{21}$$

where I_1 is the first invariant of stress tensor, and J_2 is the second invariant of deviatoric stress tensor.

The two independent damage criteria, one for tension and other for compression, are defined as:

$$\bar{\phi}^{+}\left(\bar{\tau}^{+}, r^{+}\right) = \bar{\tau}^{+} - r^{+} \leqslant 0 \tag{22}$$

and

$$\bar{\phi}^{-}\left(\bar{\tau}^{-}, r^{-}\right) = \bar{\tau}^{-} - r^{-} \leqslant 0, \tag{23}$$

where r^{+} and r^{-} are the strain-like internal variables, which act, as the current damage thresholds, being updated continuously to control the size of the expanding damage surface. The boundary damage surfaces for the effective stresses are expressed by $\bar{\phi}^{+}(\bar{\tau}^{+}, r^{+}) = 0$, and $\bar{\phi}^{-}(\bar{\tau}^{-}, r^{-}) = 0$. At the onset of the analysis, the initial value attributed to damage thresholds are $r^{+}_{0} = f_t$ and $r^{-}_{0} = f_{c0}$, where f_t is the tensile strength and f_{c0} the compression stress threshold for damage. The evolution of the damage thresholds can be expressed in a closed form, always using the highest values reached by $\bar{\tau}^{+}$ and $\bar{\tau}^{-}$, during the loading process, i.e., $r^{+} = \max\left(r^{+}_{0}, \bar{\tau}^{+}\right)$ and $r^{-} = \max\left(r^{-}_{0}, \bar{\tau}^{-}\right)$.

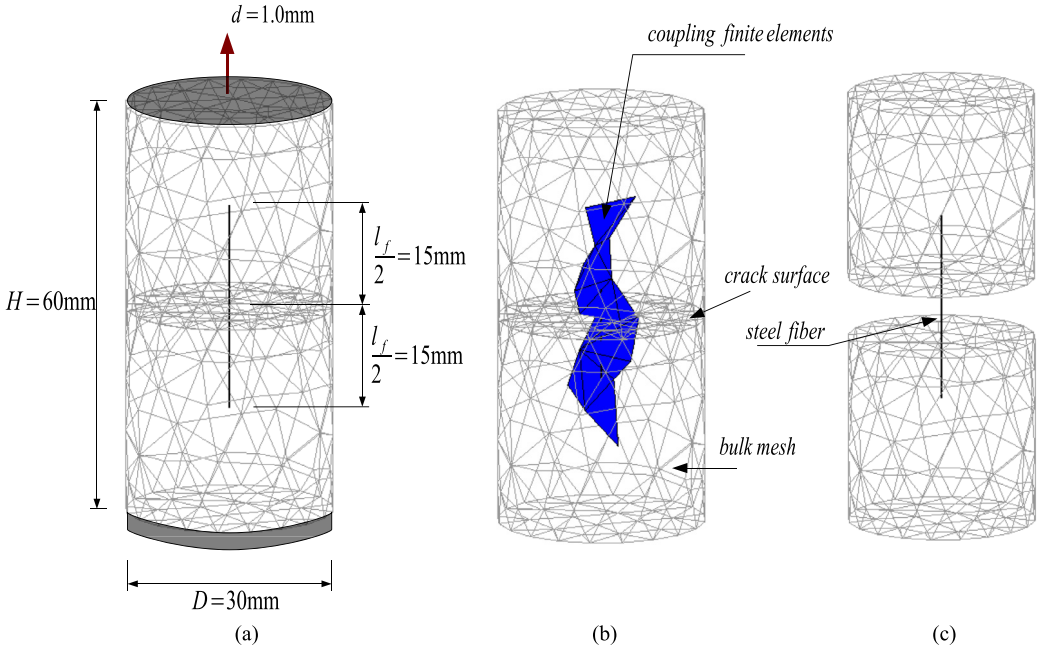

Fig. 12. 3D numerical model of the pullout test of single straight fiber embedded on both sides: (a) setup of the pullout tests, (b) detail of the coupling procedure, and (c) deformed FE mesh (with a scaling factor of 10).

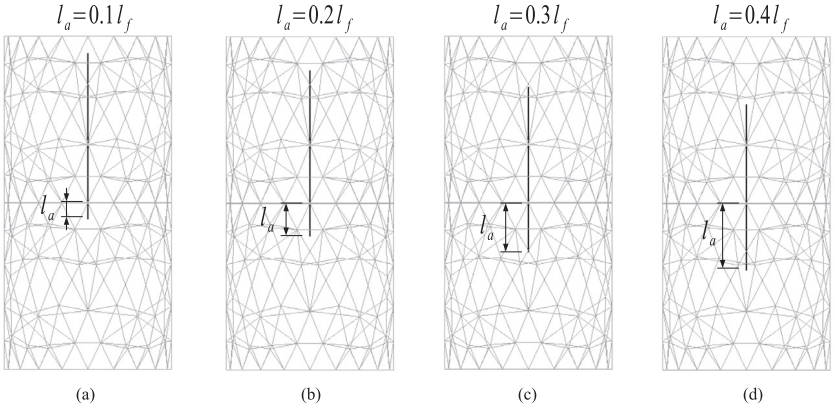

Fig. 13. Detail of the numerical models with different fiber embedment lengths: (a) $l_a = 0.1l_f$, (b) $l_a = 0.2l_f$, (c) $l_a = 0.3l_f$, and (d) $l_a = 0.4l_f$.

The evolution of the scalar damage variables are defined as:

$$d^+ = 1 - \frac{q^+(r^+)}{r^+}, \tag{24}$$

and

$$d^- = 1 - \frac{q^-(r^-)}{r^-}, \tag{25}$$

where, q^+ and q^- are the stress-like internal variables, for which two exponential expressions are adopted to define the softening behavior in tension and the hardening/softening in compression, after reaching the initial elastic limit in tension and compression, respectively:

$$q^+\left(r^+\right) = r_0^+ e^{A^+\left(1-r^+/r_0^+\right)} \tag{26}$$

and

$$q^-\left(r^-\right) = r_0^-\left(1-A^-\right) + r^- A^- e^{B^-\left(1-r^-/r_0^-\right)}. \tag{27}$$

With the above definitions, the nominal stress tensor for this model is obtained by reducing each part of the effective stress tensor, according to its respective damage variable in tension (d^+) and compression (d^-):

$$\boldsymbol{\sigma} = \left(1-d^+\right)\bar{\boldsymbol{\sigma}}^+ + \left(1-d^-\right)\bar{\boldsymbol{\sigma}}^-. \tag{28}$$

In a uniaxial tensile test, Eq. 24, with the aid of the exponential law given by the Eq. 26 is able to represent the softening in the stress-strain curve, as a process degradation of quasi-brittle materials. To satisfy the mesh objectivity condition, the energy dissipated by the material in tension must be properly related to the fracture energy of the material. Therefore, the softening parameter A^+, is derived from the ratio between the material fracture energy and the geometric factor, l_{ch}, termed characteristic length, which corresponds to the width zone where the degradation concentrates, such that:

$$\frac{1}{A^+} = \frac{1}{2\overline{H}}\left(\frac{1}{l_{ch}} - \overline{H}\right) \geqslant 0, \tag{29}$$

where $\overline{H} = f_t^2/2EG_f$ is written in terms of the tensile strength f_t, the elastic modulus E and the tensile fracture energy of the material G_f. The characteristic length depends on the spatial discretization and in this work, is assumed to be the square root of the finite element area, or the cube root of the finite element volume, for 2D and 3D problems, respectively. Note, from Eq. 29 that the introduction of the characteristic length implies a limitation on the maximum size of the finite elements employed during the mesh discretization, $l_{ch} \leqslant 1/\overline{H}$.

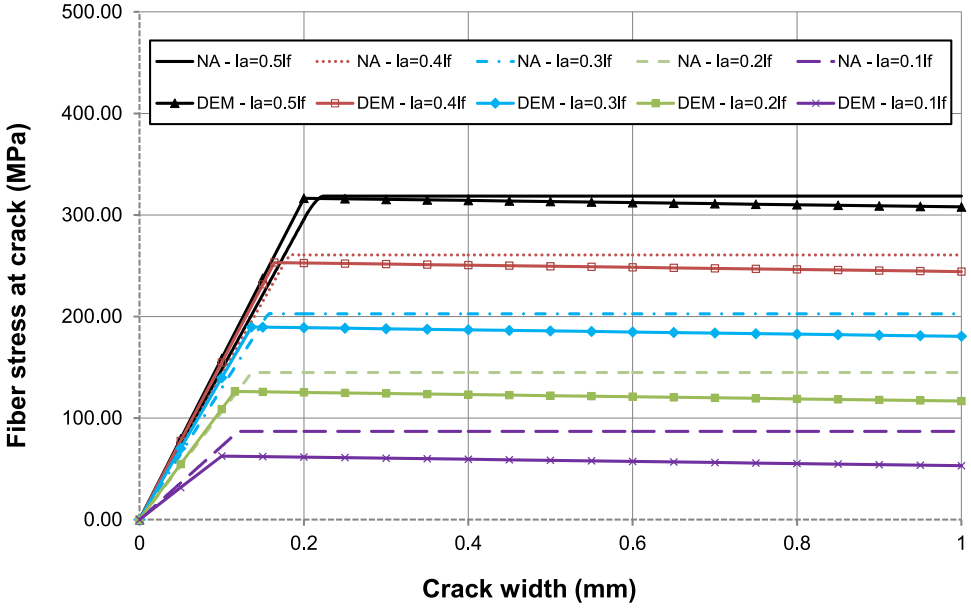

Fig. 14. Fiber stress at crack against crack width response.

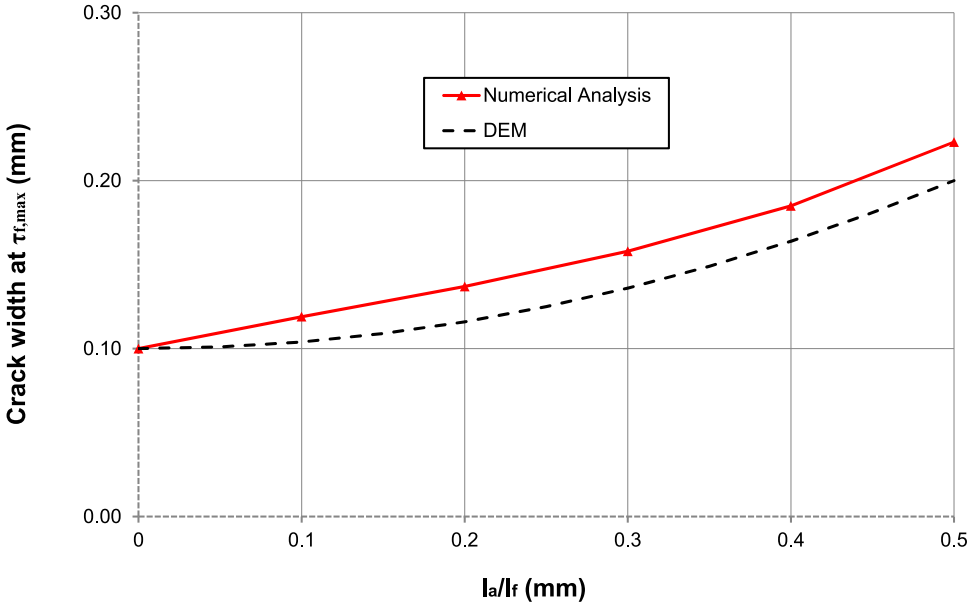

Fig. 15. Crack width at maximum pullout stress.

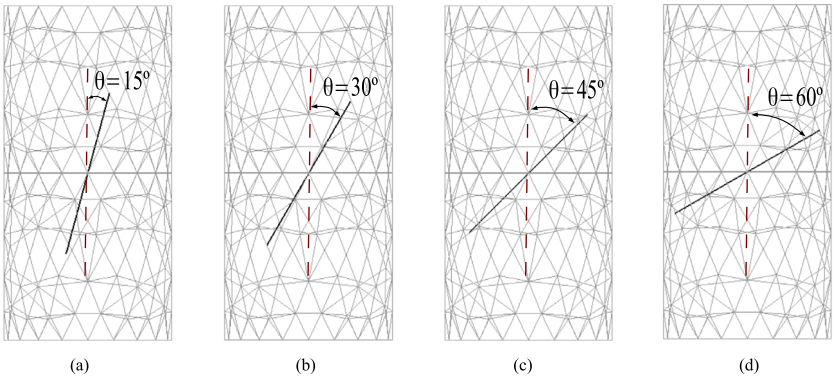

Fig. 16. Numerical models for pullout tests with different fiber inclination angles: (a) 15°, (b) 30°, (c) 45°, and (d) 60°.

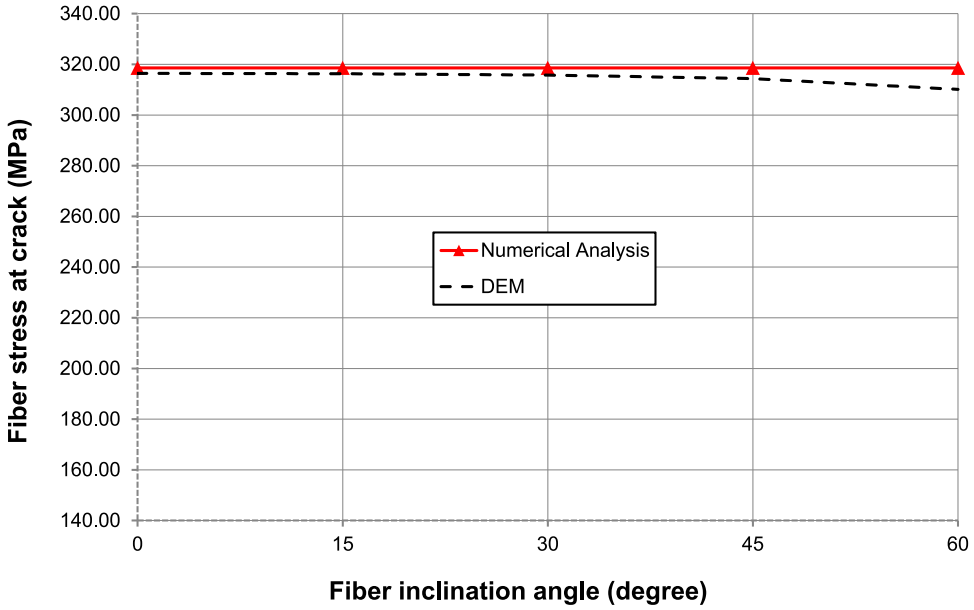

Fig. 17. Fiber stress at crack against fiber inclination angle.

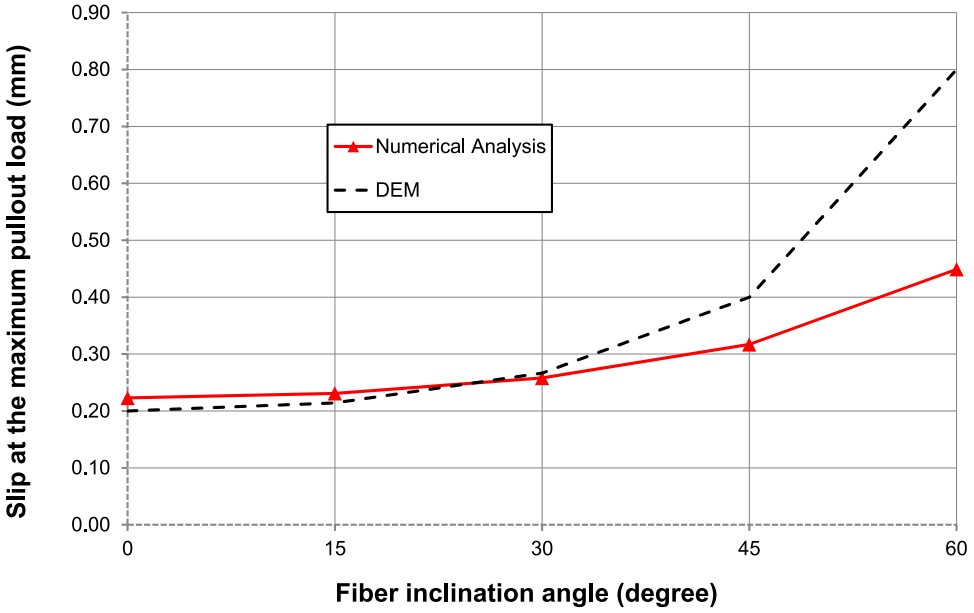

Fig. 18. Slip at frictional pullout strength against fiber inclination angle.

The parameters A^- and B^- are defined so that the stress-strain curve of the quasi-brittle material satisfies two previously selected points of a uniaxial experimental test.

3.2. Modified implicit-explicit integration scheme

A modified version of the implicit-explicit (Impl-Ex) integration scheme proposed by Oliver et al. (Oliver et al., 2006; 2008) is presented for the integration of the damage constitutive model with distinct tensile and compressive responses. The main difference between the integration scheme proposed here (Prazeres et al., 2015) and the Impl-Ex scheme proposed by Oliver et al. is the choice of the internal variables to be updated, i.e., the choice to update the inelastic strain tensor components, $\boldsymbol{\varepsilon}^d$, instead of the updating of the strain-like internal variable, r, as it is done by Oliver et al. Therefore, the method developed here is named Modified Impl-Ex, and the explicit linear extrapolation of the inelastic strain tensor components can be written as

$$\tilde{\boldsymbol{\varepsilon}}^d_{n+1} = \boldsymbol{\varepsilon}^d_n + \frac{\Delta\boldsymbol{\varepsilon}^d_n}{\Delta t_n}\Delta t_{n+1}, \tag{30}$$

where $\Delta\boldsymbol{\varepsilon}^d_n = \boldsymbol{\varepsilon}^d_n - \boldsymbol{\varepsilon}^d_{n-1}$, $\Delta t_n = t_n - t_{n-1}$, $\Delta t_{n+1} = t_{n+1} - t_n$.

The algorithm of the Modified Impl-Ex scheme is summarized in Table 4 for a representative pseudo-time step t_{n+1}. This algorithm was implemented in a closed-form, in which, given a strain tensor $\boldsymbol{\varepsilon}_{n+1}$, a stress tensor $\tilde{\boldsymbol{\sigma}}_{n+1}$ is obtained explicitly. The stress tensor $\boldsymbol{\sigma}_{n+1}$ obtained implicitly in step (vi) is used to calculate the inelastic strain tensor and its increment in step (vii). In turn, these variables calculated implicitly are used in the next step to evaluate the extrapolation of the inelastic strain tensor. To conclude, in step (ix) the explicit stress tensor is evaluated, and then used to calculate the effective algorithmic tangent operator and to fulfill the equilibrium equation.

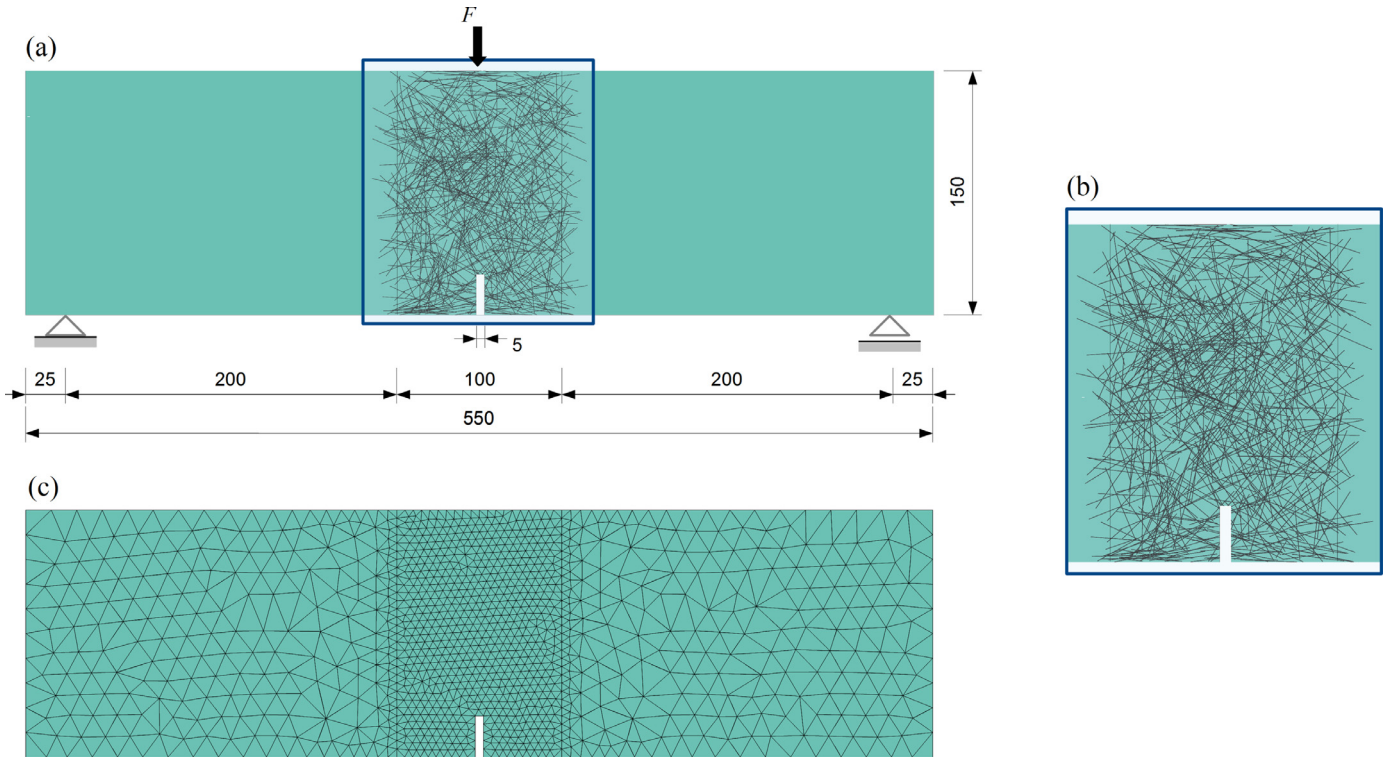

Fig. 19. 2D numerical model of the three-point bending test: geometrical properties (dimensions in mm), boundary conditions, loading and finite element mesh.

Table 4
Modified Impl-Ex integration scheme for the continuum damage model with distinct tensile and compressive responses.

INPUT: $\boldsymbol{\varepsilon}_{n+1}, \boldsymbol{\varepsilon}^d_n, \Delta\boldsymbol{\varepsilon}^d_n, r^+_n, r^-_n$

(i) Compute the effective stress tensor

$$\bar{\boldsymbol{\sigma}}_{n+1} = \mathbb{C} : \boldsymbol{\varepsilon}_{n+1}$$

(ii) Split $\bar{\boldsymbol{\sigma}}_{n+1}$ into $\bar{\boldsymbol{\sigma}}^+_{n+1}$ (according to Eq. 16) and $\bar{\boldsymbol{\sigma}}^-_{n+1}$ (according to Eq. 17)

(iii) Check loading/unloading conditions

if $\bar{\phi}^{+/-}_{n+1}\left(\bar{\tau}^{+/-}_{n+1}, r^{+/-}_n\right) < 0$, then

update damage threshold: $r^{+/-}_{n+1} = r^{+/-}_0$

else $\bar{\phi}^{+/-}_{n+1}\left(\bar{\tau}^{+/-}_{n+1}, r^{+/-}_n\right) > 0$

update damage threshold: $r^{+/-}_{n+1} = \bar{\tau}^{+/-}_{n+1}$

(iv) Update the stress-like internal variable

$q^+_{n+1}\left(r^+_{n+1}\right)$ (according to Eq. 26) and $q^-_{n+1}\left(r^-_{n+1}\right)$ (according to Eq. 27)

(v) Update the damage parameters

$$d^{+/-}_{n+1}(r^{+/-}_{n+1}) = 1 - \frac{q^{+/-}_{n+1}(r^{+/-}_{n+1})}{r^{+/-}_{n+1}}, \qquad d^{+/-}_{n+1} > 0$$

(vi) Compute the Cauchy stress tensor (implicitly)

$$\boldsymbol{\sigma}_{n+1} = \left(1 - d^+_{n+1}\right)\bar{\boldsymbol{\sigma}}^+_{n+1} + \left(1 - d^-_{n+1}\right)\bar{\boldsymbol{\sigma}}^-_{n+1}$$

(vii) Compute the inelastic strain tensor and its increment

$$\boldsymbol{\varepsilon}^d_{n+1} = \mathbb{C}(\bar{\boldsymbol{\sigma}}_{n+1} - \boldsymbol{\sigma}_{n+1}) \text{ and } \Delta\boldsymbol{\varepsilon}^d_{n+1} = \boldsymbol{\varepsilon}^d_{n+1} - \boldsymbol{\varepsilon}^d_n$$

(viii) Compute explicit linear extrapolation of the inelastic strain tensor

$$\tilde{\boldsymbol{\varepsilon}}^d_{n+1} = \boldsymbol{\varepsilon}^d_n + \frac{\Delta\boldsymbol{\varepsilon}^d_n}{\Delta t_n}\Delta t_{n+1} = \boldsymbol{\varepsilon}^d_n + \frac{\left(\boldsymbol{\varepsilon}^d_n - \boldsymbol{\varepsilon}^d_{n-1}\right)}{\left(t_n - t_{n-1}\right)}\left(t_{n+1} - t_n\right)$$

(ix) Compute the stress tensor (explicitly)

$$\bar{\boldsymbol{\sigma}}_{n+1} = \mathbb{C}\left(\boldsymbol{\varepsilon}_{n+1} - \tilde{\boldsymbol{\varepsilon}}^d_{n+1}\right)$$

OUTPUT: $\bar{\boldsymbol{\sigma}}_{n+1}, \boldsymbol{\varepsilon}^d_{n+1}, \Delta\boldsymbol{\varepsilon}^d_{n+1}, r^+_{n+1}, r^-_{n+1}$

Compute the effective algorithmic tangent operator

$$\tilde{\mathbb{C}}^{\tan}_{n+1} = \frac{\partial\bar{\boldsymbol{\sigma}}_{n+1}}{\partial\boldsymbol{\varepsilon}_{n+1}} = \mathbb{C}$$

3.3. Example: uniaxial loading test

To illustrate the behavior of the damage constitutive model adopted in the continuous approach, a uniaxial test is performed. Fig. 5 shows the test setup composed by two three-node triangular finite elements in plane stress condition with an out-of-plane thickness of 100mm. The parameters adopted are: Young's modulus $E = 30.0$GPa; Poisson's ratio $\nu = 0.2$; fracture energy $G_f = 0.1$N/mm; tensile strength $f_t = 3.0$MPa; compression stress threshold for damage $f_{c0} = 15$MPa and the compressive parameters $A^- = 1.0$ and $B^- = 0.89$.

To describe the behavior of the constitutive model under tension and compression, the loading history in Fig. 6 was considered. First, the elements are stretched (Fig. 5(a)) during the interval 1–2. Then, a reversed load (Fig. 5(b)) is applied in the interval 2–3.

Fig. 7 illustrates the response obtained. The path A-B-C describes the response in tension when the elements are stretched. The behavior is described by a linear relation until the tensile

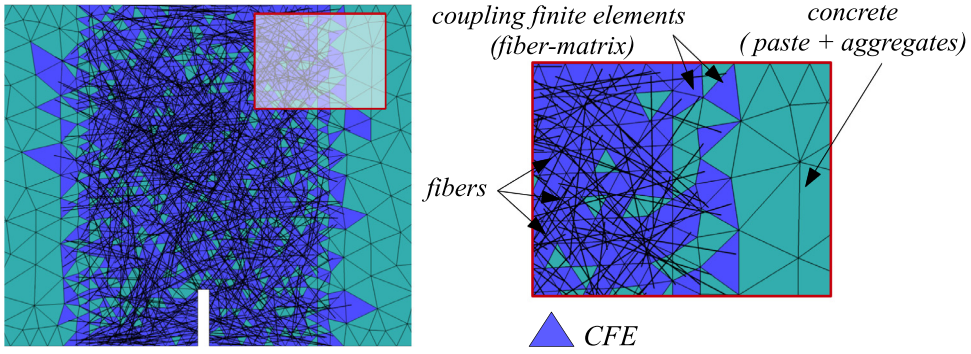

Fig. 20. Detail of the coupling finite elements.

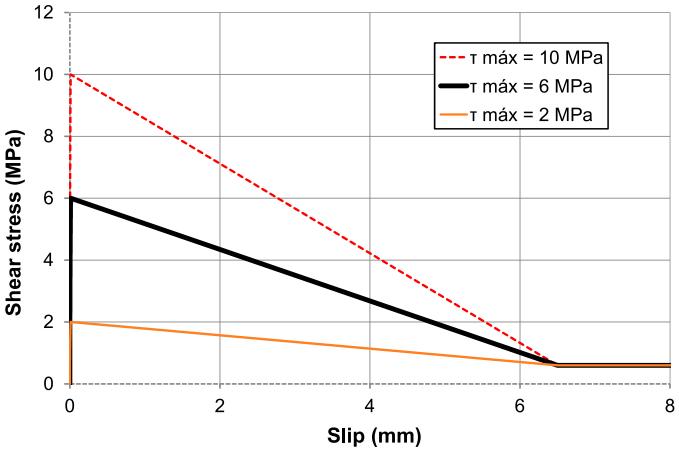

Fig. 21. Bond-slip models adopted to describe the concrete-fiber interaction.

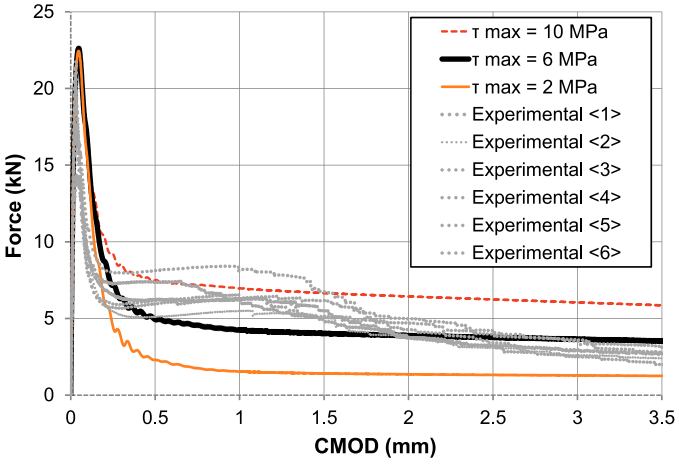

Fig. 22. Force x CMOD curves. Comparison between numerical and experimental responses.

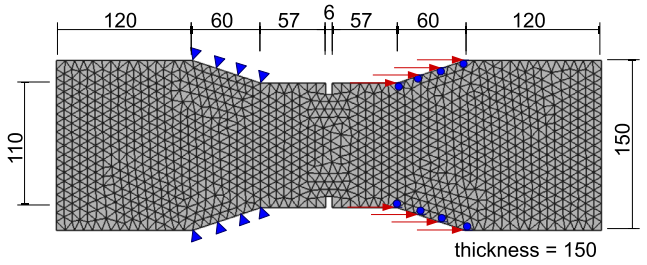

Fig. 24. 2D numerical model of the direct tension tests carried out by Baez (2014) on notched specimens: geometrical properties (dimensions in mm), boundary conditions, loading and finite element mesh.

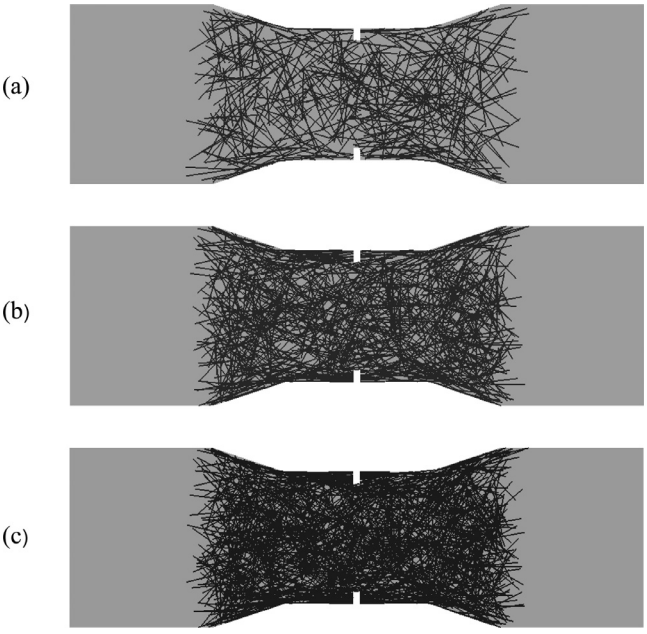

Fig. 25. Fiber distribution in the direct tension test specimens for : (a) $V_f = 0.5\%$ (506 fibers), (b) $V_f = 1.0\%$ (1545 fibers) and (c) $V_f = 1.5\%$ (1545 fibers).

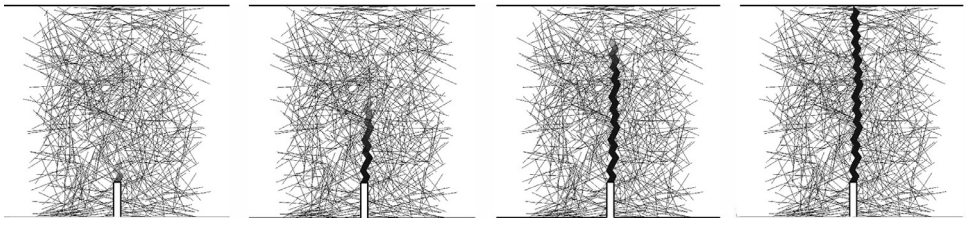

Fig. 23. Crack propagation process for the case with $\tau_{max} = 10.0$MPa.

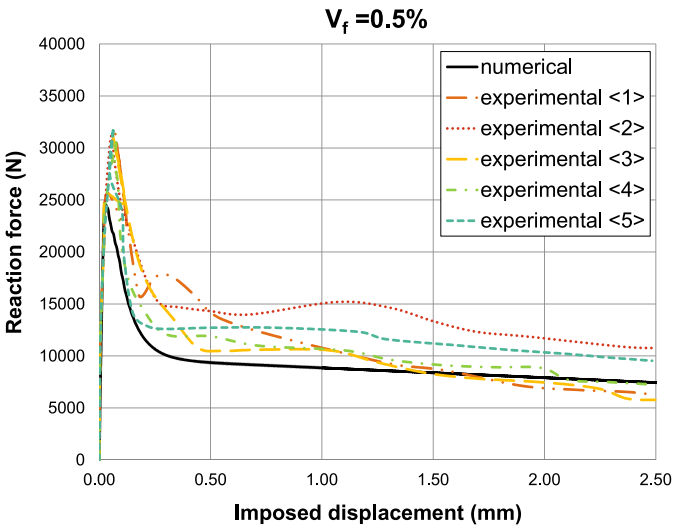

Fig. 26. Force x displacement curves. Comparison between numerical and experimental responses for $V_f = 0.5\%$.

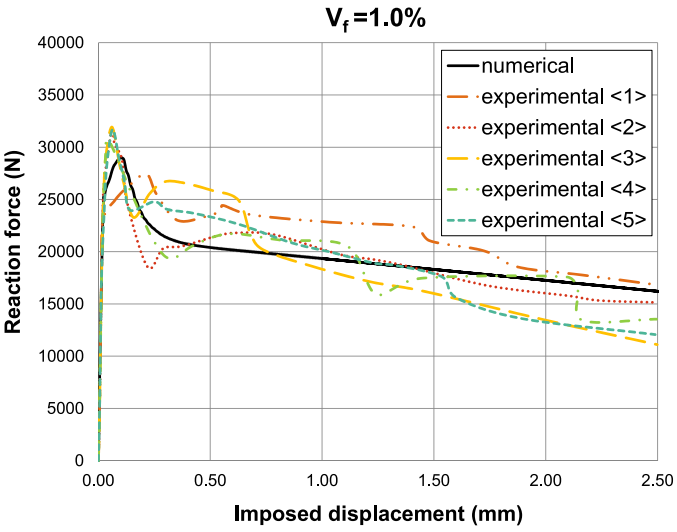

Fig. 27. Force x displacement curves. Comparison between numerical and experimental responses for $V_f = 1.0\%$.

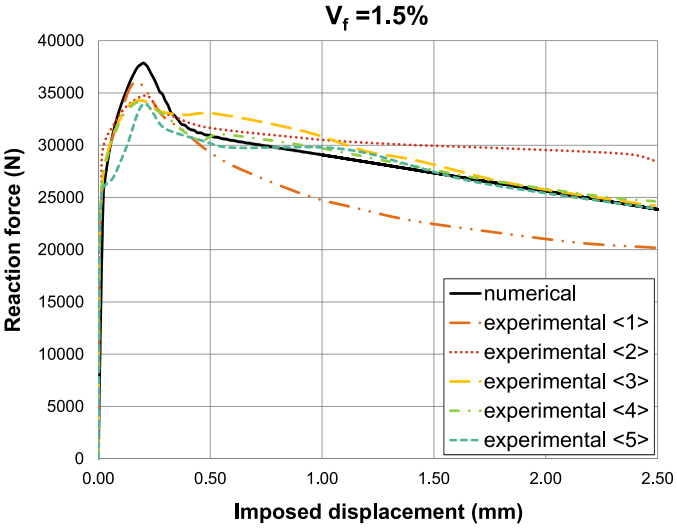

Fig. 28. Force x displacement curves. Comparison between numerical and experimental responses for $V_f = 1.5\%$.

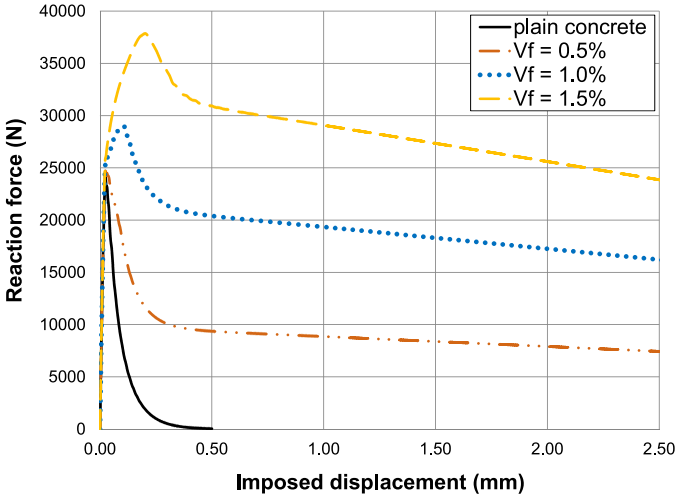

Fig. 29. Numerical analyses using damage model. Plain concrete and steel fiber reinforced concrete with steel fiber volume fractions of 0.5, 1.0 and 1.5%.

strength of the material is achieved (point B) followed by a strain softening regime that is defined by the fracture energy adopted. Then, the imposed displacement is reversed so that secant unloading (path C-A), recovery of the stiffness and damage in compression occur (path A-D-E). Note that the point D is the compression stress threshold for damage.

4. Applications

This section presents three examples selected to demonstrate the advantages of the new strategy for modeling steel fiber reinforced concrete.

4.1. Pullout behavior of steel fibers

The non-rigid coupling approach (non-perfect bond) developed is assessed through the numerical analysis of a set of pullout tests of steel fibers. This study aims to verify the capability of the coupling strategy in modeling fiber-matrix interaction, taking into account the main factors influencing its behavior, such as type of steel fiber, embedment length and inclination angle.

The results are compared to the ones obtained by using the analytical formulas of the Diverse Embedment Model (DEM) (Lee et al., 2011). This comparison is very interesting because the DEM represents a more comprehensive approach currently available for calculating the response of steel fiber reinforced concrete (SFRC) members subjected to tension and its formulation is derived from pullout tests of single steel fibers under different embedment lengths and inclination angles (Lee et al., 2011).

4.1.1. Fiber embedded on one side

The first pullout configuration considered in the development of the DEM consists of a single straight fiber with a circular cross-section embedded on one side. To solve the second-order differential equation corresponding to the bond slip behavior, a bilinear bond stress-slip relationship between the fiber and the concrete matrix was assumed, with frictional pullout strength of $\tau_{f,max} =$ 3.0MPa and slip at frictional pullout strength of $s_f = 0.1$mm. Additionally, the tributary area of concrete considered effective is based on a prism diameter of 15 times the fiber diameter. It is used a straight steel fiber of length $l_f = 30$mm, diameter $d_f = 0.565$mm, whose behavior is described by an elastic perfectly plastic model, with Young's modulus of $E_f = 210$GPa and yield stress of $\sigma_y =$

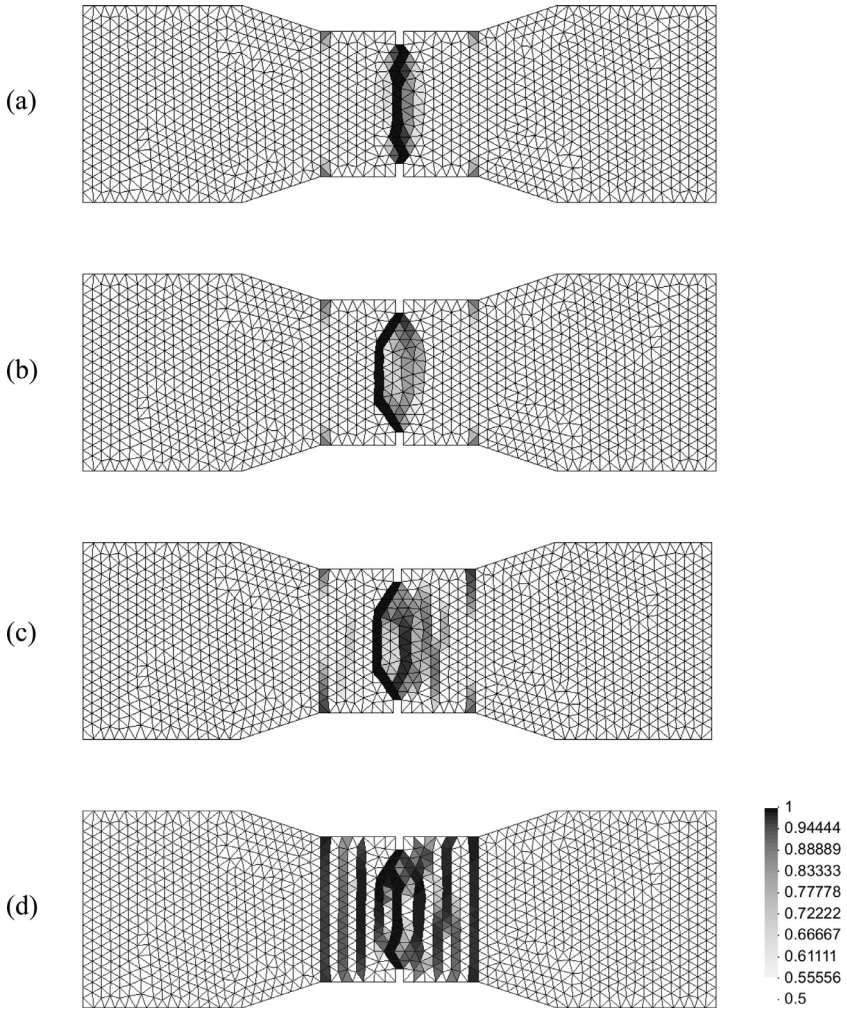

Fig. 30. Failure patterns (damage distribution) at the end of the analyses for: (a) plain concrete, (b) $V_f = 0.5\%$, (c) $V_f = 1.0\%$ and (d) $V_f = 1.5\%$. (damage factor varying from 0.5 to 1).

345MPa. The fiber is embedded in a linear elastic matrix material, with Young's modulus of $E_c = 32,617$MPa and Poisson's ratio of $\nu_c = 0.18$. Thus, to simulate numerically this pullout test, the finite element model illustrated in the Fig. 8 was constructed.

The fiber is discretized using 10 two-node (truss) elements, embedded in the cylindrical specimen discretized with 608 four-node tetrahedral finite elements. The fiber and matrix are modeled using an elastoplastic and elastic material model, respectively, with the same parameters adopted in the analysis by the DEM. These two independent meshes are coupled using 6 five-node tetrahedral coupling finite elements, as shown in Fig. 8(b). The concrete-fiber interaction is described by the damage model presented in the Section 2.3.3. In order to describe the same bilinear bond stress-slip relationship assumed by the DEM, the model depicted in Fig. 9 was adopted for the interface, which may be described assuming:

$$\tau(s) = \begin{cases} \tau_{max}\left(\frac{s}{s_1}\right) & \text{if} \quad s \leq s_1 \\ \tau_{max} & \text{if} \quad s > s_1 \end{cases}, \tag{31}$$

that considering the relationship $q(r) = \tau(r/c_n)$, may be also described in terms of the stress- and strain-like internal variable as:

$$q(r) = \begin{cases} \tau_{max}\left(\frac{r/c_n}{s_1}\right) & \text{if} \quad r/c_n \leq s_1 \\ \tau_{max} & \text{if} \quad r/c_n > s_1 \end{cases} \tag{32}$$

The following values are adopted for the interface parameters: $c_n = 10^3$MPa/mm, $\tau_{\max} = 3.0$MPa, and $s_1 = 0.1$mm. To avoid the separation and penetration between the fiber and matrix in the direction normal to fiber, $\tilde{c} = 10^9$MPa/mm was assumed.

In the numerical analysis, a prescribed vertical displacement is imposed at the free end of the fiber (see Fig. 8(a)), and a fixed boundary condition is considered at the bottom of the cylindrical specimen. Fig. 10 illustrates the results obtained in terms of fiber stress against the fiber slip at crack. As can be seen, the result obtained by numerical analysis is identical to that obtained by the DEM, showing that the strategy adopted for the interface is able to reproduce the fiber-matrix interaction. Moreover, the variation of the slip along the fiber obtained numerically is also identical to that obtained by the DEM, as shown in Fig. 11.

4.1.2. Fiber embedded on both sides

Here, the same geometrical and mechanical properties adopted in the previous analysis with fiber embedded on one side are considered. First, in order to verify the influence of the fiber embedded length, a set of tests with fiber embedded on both sides perpendicular to the crack surface is performed. Fig. 12 shows the numerical model constructed for the numerical analysis, with a fiber embedded length of $l_a = 0.5l_f$. Note in this figure that a crack is defined at the central part of the cylindrical specimen, parallel to the base and top surfaces of the cylinder. Thus, the interaction be-

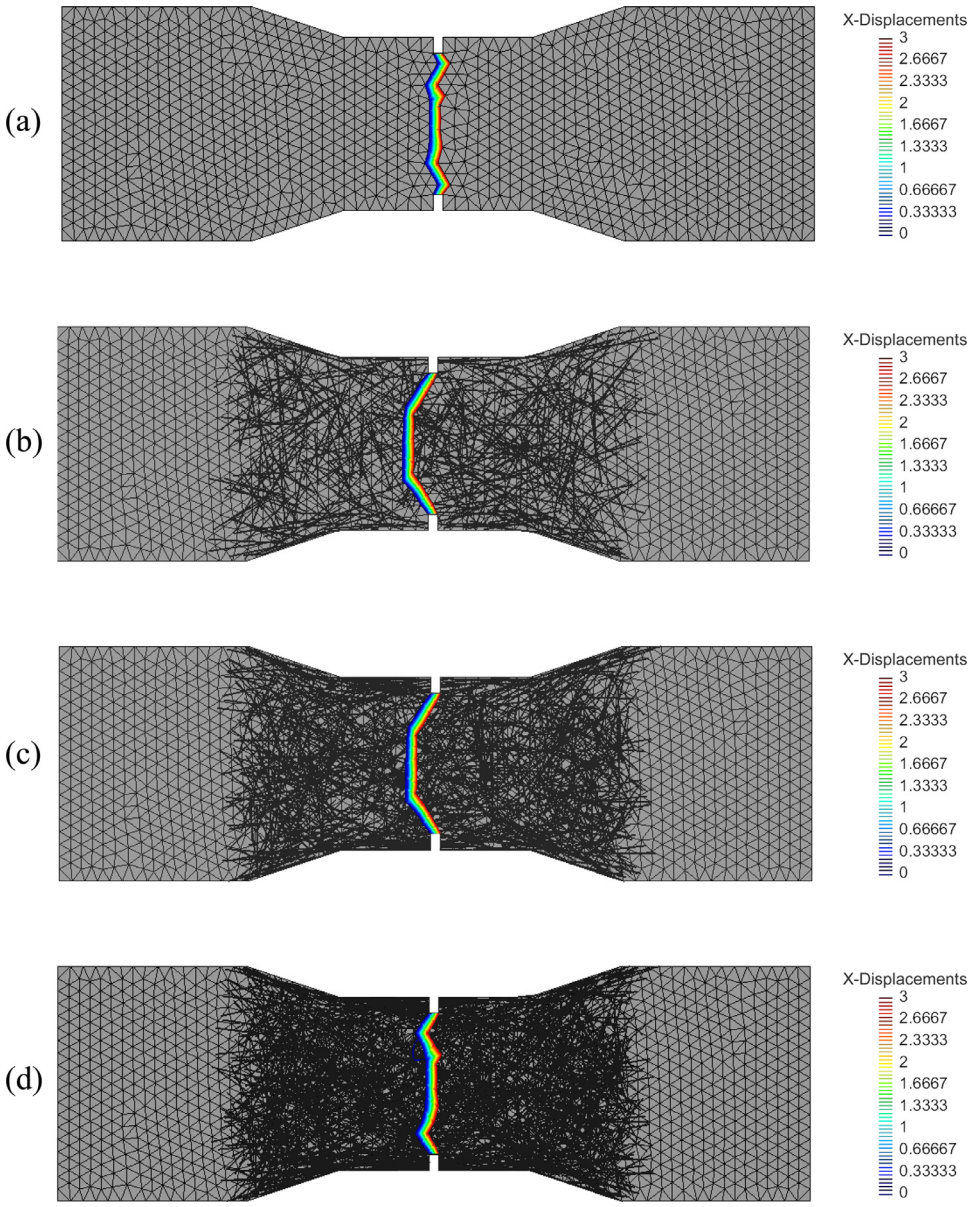

Fig. 31. Horizontal displacement contour (mm): (a) plain concrete; (b) $V_f = 0.5\%$, (c) $V_f = 1.0\%$ and (d) $V_f = 1.5\%$.

tween the top and bottom parts of the cylindrical specimen during the pullout tests is driven by the fiber-matrix interface.

For the discretization in finite elements, the same mesh refinement applied to construct the model with one fiber embedded on one side was employed. The coupling procedure between the non-matching meshes is shown in Fig. 12(b). As boundary conditions, the bottom surface of the cylinder is fixed, whereas a prescribed vertical displacement at the top surface is imposed. The other pullout tests considered with different fiber embedment lengths are illustrated in Fig. 13.

For this pullout test configuration, based on the DEM, the tensile stress of the fiber at the crack can be calculated by

$$\sigma_{f,cr} = \frac{4\tau_{short}(l_a - s_{short})}{d_f}, \tag{33}$$

where s_{short} is the slip at crack for the shorter embedded part of the fiber and τ_{short} is the corresponding frictional bond stress, which can be obtained by

$$\tau_{short} = \begin{cases} \frac{w_{cr}}{w_{p0}}\tau_{f,max} & \text{if} \quad w_{cr} \le w_{p0} \\ \tau_{f,max} & \text{if} \quad w_{cr} > w_{p0} \end{cases} \tag{34}$$

In the Eq. 34, w_{p0} is the crack width at the maximum pullout stress, defined as

$$w_{p0} = s_f\left[1 + 4\left(\frac{l_a}{l_f}\right)^2\right], \tag{35}$$

where s_f is the slip at the frictional pullout strength.

Fig. 14 compares the variation of the fiber stress as a function of the crack width for the different fiber embedment lengths. In general, the results obtained in the numerical analyses are in good agreement with those obtained by the DEM. Note that, as expected, for the case with $l_a = 0.5l_f$, the crack width is about twice of that obtained with fiber embedded on one side. The difference between responses increases as the fiber embedment length decreases.

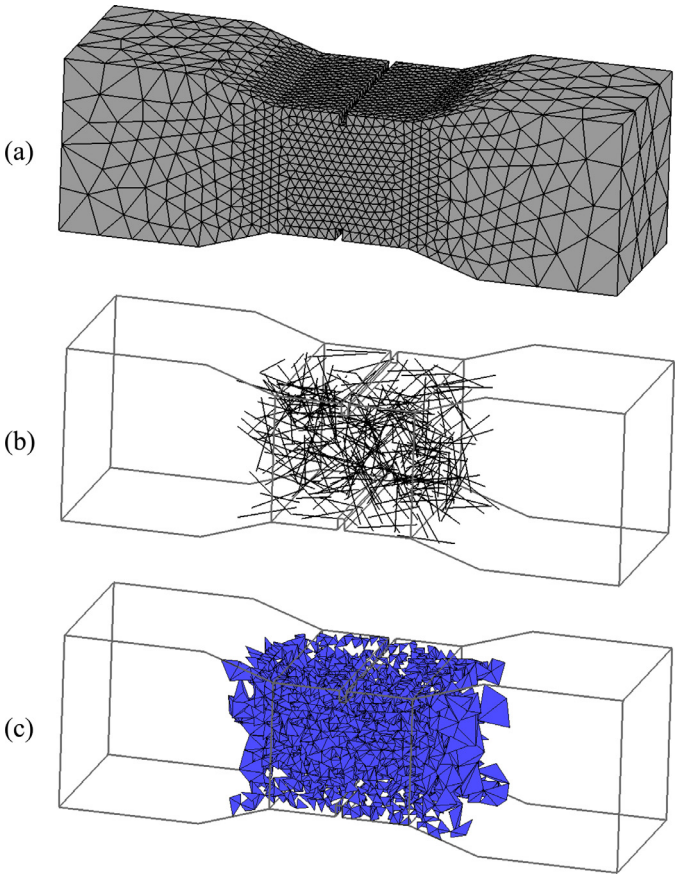

Fig. 32. 3D finite element mesh of the direct tension test: (a) concrete; (b) cloud of fibers ($V_f = 0.5\%$) and (c) coupling finite elements. .

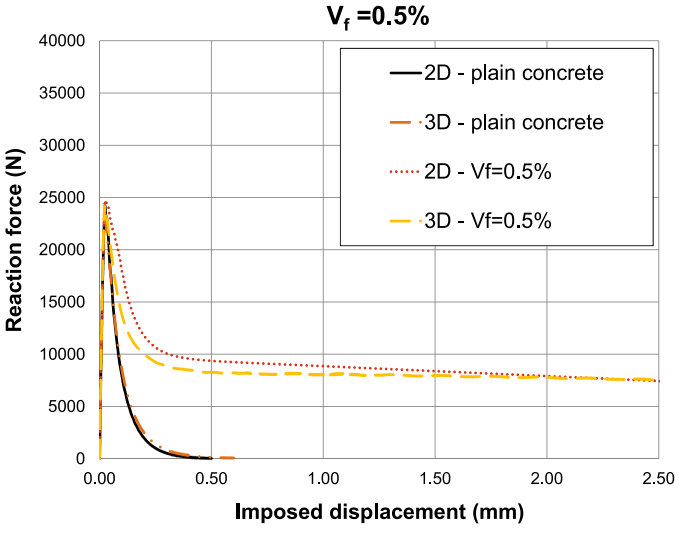

Fig. 33. Comparison between force x displacement curves obtained for 2D and 3D numerical analyses using damage model of steel fiber concrete with fiber volume fraction of $V_f = 0.5\%$.

Regarding the crack width at maximum pullout stress, the same tendency is observed, as can be seen in Fig. 15. However, the values obtained by the numerical analyses are slightly larger than those obtained by the DEM.

To investigate the effect of fiber orientation, pullout tests of fibers with inclination angles from 15° to 60° were considered. Fig. 16 shows the models constructed for the numerical analyses.

Based on the DEM, the tensile stress of the fiber at the crack for an arbitrary inclination angle can be calculated by the Eq. 33, where the frictional bond stress, τ_{short}, is given by

$$\tau_{short} = \begin{cases} \frac{w_{cr}}{w_{p\theta}}\tau_{f,max} & \text{if} \quad w_{cr} \leq w_{p\theta} \\ \tau_{f,max} & \text{if} \quad w_{cr} > w_{p\theta} \end{cases}, \tag{36}$$

and the crack width at bond strength for fiber inclination angle θ is defined as

$$w_{p\theta} = \frac{s_f\left[1 + 4\left(\frac{l_a}{l_f}\right)^2\right]}{\cos^2\theta}. \tag{37}$$

According to DEM approach, by assuming that the crack width is given by the sum of the slips from longer and shorter embedded sides ($w_{cr} = s_{long} + s_{short}$), the maximum stress that the fiber experiences can be estimated for a given w_{cr} as follows

$$\sigma_{f,cr,exp} = \frac{4w_{cr}}{w_{p\theta}}\left[l_a - \frac{(l_a - s_{short})w_{cr} - w_{cr}^2}{l_f - 2w_{cr}}\right]\frac{\tau_{f,max}}{d_f}, \tag{38}$$

where w_{cr} is not longer than $w_{p\theta}$. The Eq. 38 was developed from Eq. 33 and considering $s_{short} = \frac{(l_a - s_{short})w_{cr} - w_{cr}^2}{l_f - 2w_{cr}}$.

Fig. 17 illustrates the results obtained in terms of fiber stress at crack for different fiber inclination angles at maximum pullout load, in which $w_{cr} = w_{p\theta}$. The numerical results are very similar to those calculated using the equation proposed in the DEM. For these same tests, the slip at frictional pullout strength is plotted against each fiber inclination angle, as shown in Fig. 18. For angles less than 30° the results obtained are in very good agreement, while for angles larger than 30°, the results obtained are slightly larger than those obtained by the DEM, which was given by the following equation:

$$s_{f\theta} = \frac{s_f}{\cos^2\theta}. \tag{39}$$

In this work, as the influence of the fiber-matrix interaction is accounted on the constitutive model adopted to describe the bond-slip behavior, the analyses performed above for straight fibers are valid for any type of fibers. Thus, for other types of fibers, as for example, end-hooked steel fibers, the effect of the mechanical anchorage provided by the end hook may be accounted into the bond-slip model adopted.

4.2. Three-point bending test - EN 14651

Three-point bending tests performed experimentally in the Laboratory of Structures and Structural Materials (LEM) at the University of Sao Paulo (USP) are numerically simulated. The tests are performed according to the recommendations of EN 14651 (EN 14651, 2007) and all the beams have 20kg/m^3 of steel fibers.

Fig. 19 shows the numerical model with 7508 degrees of freedom. As can be seen in this figure, only the fibers around the center of the beam are considered in the analyses in order to avoid high computational costs. The analyses are carried out considering plane stress conditions with an out-of-plane thickness of 150mm. An incremental vertical force is applied on the centre-point of the specimen.

The concrete is discretized in 2201 three-node triangular finite elements. The continuum damage model presented in Section 3.1 is applied for modeling the failure processes with the following parameters: Young's modulus $E = 37,500$MPa; Poisson's ratio $\nu = 0.2$; fracture energy $G_f = 0.1$N/mm; tensile strength $f_t = 5$MPa; compression stress threshold for damage $f_{c0} = 46.0$MPa and compressive parameters $A^- = 1.0$ and $B^- = 0.89$.

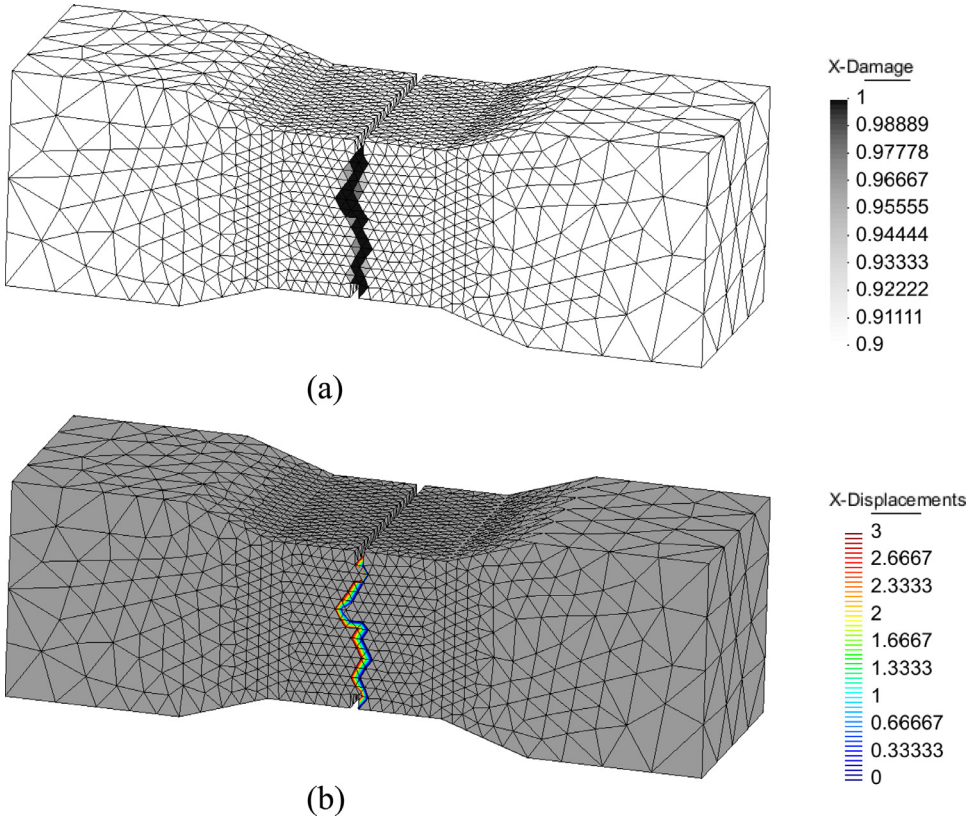

Fig. 34. Failure pattern obtained using damage model with $V_f = 0.5\%$: (a) damage and (b) horizontal displacement contour field.

The hooked steel fibers used in the experimental tests were the Dramix®65/35 (type A-I), with length of $l_f = 35.0$mm and diameter of $d_f = 0.55$mm. The steel fibers are discretized using two-node (one-dimensional) truss finite elements. A total of 1264 truss elements with elastic perfectly plastic constitutive model with Young's modulus of $E_s = 210$GPa and yield stress of $\sigma_y = 1345$MPa.

The coupling between the independent meshes of the concrete and steel fibers are carried out by 2579 four-node triangular coupling finite elements, as illustrated in Fig. 20. The fiber-concrete interaction is described using three different the bond-slip models (see Fig. 21) with the following parameters: $\tau_{\max} = 10.0$MPa (case 1), $\tau_{\max} = 6.0$MPa (case 2), $\tau_{\max} = 2.0$MPa (case 3), $\tau_f = 0.6$MPa, $\alpha = 0.4$, $s_1 = 0.01$mm, $s_2 = 6.5$mm, $c_n = 10^3$MPa/mm and $\tilde{c} = 10^9$MPa/mm. The parameters s_1 and s_2 were calibrated to describe the descending part of the experimental responses.

Fig. 22 shows the force x CMOD curves obtained for the three bond-slip models considered. As can be seen, the parameters obtained to describe the fiber-concrete interaction have strong influence on the response and the numerical model is able to reproduce the results obtained experimentally. However, as the effect of the end hooks is accounted along the length of the fiber into the bond-slip model, the bump effect usually found in hooked fiber concretes cannot be observed in the numerical responses. The crack propagation process for the first case ($\tau_{\max} = 10.0$MPa) is shown in Fig. 23.

4.3. Direct tension test

In this example a series of experimental direct tension tests carried out by Baez (2014) on notched specimens with steel fiber volume fractions of 0.5, 1.0 and 1.5% are numerically analyzed. Five specimens were tested for each fiber volume fraction in order to study the variability of the results.

Fig. 24 shows the geometrical properties, boundary conditions, and finite element mesh employed for the 2D numerical analyses performed. The analyses are carried out considering plane stress conditions with an out-of-plane thickness of 150mm. A horizontal displacement of $\delta = 2.5$mm on the right side of the specimen is imposed incrementally.

The hooked steel fibers used in the experimental tests were the Dramix®RL 45/50 BN with length of $l_f = 50.0$mm and diameter of $d_f = 1.05$mm. The steel fibers are discretized using two-node (one-dimensional) truss finite elements. A total of 1282, 2558 and 3852 truss elements were employed in the models with steel fiber volume fractions of 0.5, 1.0 and 1.5%, respectively. An elastic perfectly plastic constitutive model, with Young's modulus of $E_s = 200$GPa and yield stress of $\sigma_y = 520$MPa was used to describe their behavior. The distributions of the fibers for the three cases are depicted in Fig. 25. As can be noted in this figure, only the fibers around the center of the specimen are considered in the analyses. A previous study of this example demonstrated that the fibers outside the fracture plane have almost no influence on final response.

The concrete bulk is discretized into 2312 three-node triangular finite elements for all the cases. The continuum damage model presented in Section 3.1 is applied for modeling the failure processes with the following parameters: Young's modulus $E = 18,101$MPa; Poisson's ratio $\nu = 0.23$; fracture energy $G_f = 0.100$N/mm; tensile strength $f_t = 1.72$MPa; compression stress threshold for damage $f_{c0} = 20.0$MPa and compressive parameters $A^- = 1.0$ and $B^- = 0.89$.

The coupling between the independent meshes of the concrete bulk and steel fibers are carried out by four-node triangular coupling finite elements with the bond-slip model out-

lined in Section 2.3.3. To describe the concrete-steel fiber interaction, the following parameters were adopted: $\tau_{max} = 9.0$MPa, $\tau_f = 1.5$MPa, $\alpha = 0.4$, $s_1 = 0.01$mm, $s_2 = 3.5$mm, $c_n = 10^3$MPa/mm and $\tilde{c} = 10^9$MPa/mm.

Fig. 26 to Fig. 28 show the force x displacement curves obtained for the different fiber volume fractions considered. As can be seen, the numerical results are in good agreement with those obtained experimentally by Baez (2014).

The numerical results obtained for the different fiber volume fractions are also plotted in Fig. 29. In addition, the response for a specimen of plain concrete is also plotted in this figure in order to become clear the contribution of the fibers. The failure patterns for all these cases are illustrated in Fig. 30. Note that for the plain concrete a localized damage is observed, whereas for the specimens with steel fibers a widespread damage composed by a main crack and secondary cracks is obtained, as observed in the experimental tests. This is justified by the stress transfer between cracks provided by the fibers. To illustrate the process of crack localization (main crack), the horizontal displacement contour is plotted, as shown in Fig. 31. In all the fiber contents considered, the displacement has been localized near the plane connecting the notches, despite of a widespread damage be observed by increasing the volume of fibers (see Fig. 30).

3D numerical analysis is also performed for the specimen with $V_f = 0.5\%$. Figs. 32(a) and (b) show the finite element mesh used for the concrete bulk and the distribution of fibers employed in the analysis, respectively. The coupling elements used in this analysis are illustrated in Fig. 32. In addition, to illustrate the effect of the fibers, the specimen of plain concrete is also simulated.

A comparison between the 2D and 3D analyses in terms of force x displacement curves for the case of $V_f = 0.5\%$ is shown in Fig. 33. As can be noted the 2D and 3D results for $V_f = 0.5\%$ are in good agreement.

The failure pattern obtained for the case with $V_f = 0.5\%$ is shown in Fig. 34.

5. Conclusions

In this work, a numerical model for SFRC has been proposed. In this model, the material is composed by three phases: concrete, discrete discontinuous fibers and concrete-fiber interface. To obtain this model, the coupling technique proposed by Bitencourt Jr. et al. (2015) is applied. Thus, the finite element meshes of the concrete and of a cloud of fibers can be generated independently, avoiding homogenized models and conformal meshes.

The coupling technique adopted for coupling non-matching meshes based on the use of coupling finite elements demonstrated to be highly versatile because it can be used for coupling meshes composed of different types of finite elements for two and three-dimensional problems.

From the fiber content and the geometrical properties of both the steel fiber and concrete specimen, a cloud of fibers is generated using an isotropic uniform random distribution while considering the wall effect of the mold, according to the algorithm proposed by Cunha (2010). For the numerical analyses performed in this research, good results in terms of structural and cracking responses have been obtained by employing the distribution proposed by this algorithm.

Continuum damage models are used for modeling the quasi-brittle behavior of the concrete and the concrete-fiber interaction. For the first, a model with two independent scalar damage variables for describing the composite behavior under tension and compression is employed, while the non-rigid version of coupling scheme proposed by Bitencourt Jr. et al. (2015) is used to describe the relationship between the shear stress and the relative sliding between the concrete and fibers. In addition, to increase the computability and robustness of the continuum damage models employed in this research, an implicit-explicit integration scheme is used. For the concrete-fiber interface, the same procedures proposed by Oliver et al. (Oliver et al., 2006; 2008) is adopted, and for the continuum damage model used to simulate the failure process in concrete, the inelastic strain tensor components are chosen to be updated instead of updating the strain-like internal variable, as proposed by Oliver et al. The use of this integration scheme was found to be very robust since no problems related to convergence during the nonlinear analyses were found. The guaranteed convergence and robustness of the implicit-explicit algorithm result from the obtained positive definite algorithmic tangent operator.

In general, the results obtained in numerical analyses demonstrated that the proposed numerical approach is able to represent, efficiently, qualitatively and quantitatively, the main failure mechanisms of SFRC. The main advantage obtained using the proposed methodology is that the main factors that influence the behavior of SFRC can be considered separately, including the complex behavior of the concrete-fiber interaction, which plays an important role in the material failure process.

In the first example a set of numerical pullout tests considering different types of fibers, embedment lengths and inclination angles is also performed. For comparison with the basic equations of the DEM proposed by Lee et al. (2011), the same pullout test configurations described in the development of this model are adopted. The results obtained with the proposed numerical approach are in very good agreement with those obtained by the DEM, demonstrating that the proposed approach is very appealing for use in modeling SFRC with a discrete treatment of fibers.

A three-point bending beam is numerically simulated in the second example. In the lack of pullout test results, three curves to describe the concrete-fiber interaction were adopted in order to compare the results with those obtained experimentally in the Laboratory of Structures and Structural Materials at the University of Sao Paulo. The results show that the concrete-fiber interaction has strong influence in the response of the composite showing that pullout test is important to understand the behavior of this type of composite.

In the last example, a series of experimental direct tension tests carried out by Baez (2014) on notched specimens with steel fiber volume fractions of 0.5, 1.0 and 1.5% are numerically analyzed. A previous study of this example demonstrated that the fibers outside the fracture plane have almost no influence on final response. Thus, fibers outside the fracture plane were removed to avoid high computational costs. The load deflection curves obtained are in very good agreement with those obtained by Baez (2014). Moreover, as occurred in the previous examples, the continuum damage model used was able to capture the process of failure.

Finally, the numerical approach developed may be very useful in future researches and the numerical tool may be the base source code for the developments to be made in the field of failure processes in fiber reinforced cementitious composites.

Acknowledgments

The authors wish to acknowledge the financial support of the National Council for Scientific and Technological Development - Conselho Nacional de Desenvolvimento Científico eTecnológico (429552/2016-5), Sao Paulo Research Foundation - Fundação de Amparo Pesquisa do Estado de São Paulo (2009/07451-2 and 2012/05430-0) and Coordination for the Improvement of Higher Education Personnel - Coordenação de Aperfeiçoamento de Pessoal de Nível Superior.

References

Baez, F.A.L., 2014. Modelo numerico del comportamiento inelastico del concreto reforzado con fibras cortas de acero Ph.D. Thesis. . Universidad Nacional de Colombia.

Bazănt, Z.P., Oh, B.H., 1983. Crack band theory for fracture of concrete. Matériaux et Constructions 93 (16), 155–177.

Bentur, A., Mindess, S., 2007. Fibre reinforced cementitious composites. Modern Concrete Technology Series.

Bitencourt Jr., L.A.G., Manzoli, O.L., Prazeres, P.G.C., Rodrigues, E.A., Bittencourt, T.N., 2015. A coupling technique for non-matching finite element meshes. Comput. Methods Appl. Mech. Eng. 290, 19–44. http://www.sciencedirect.com/science/article/pii/S0045782515000870.

Bitencourt Jr., L.A.G., Manzoli, O.L., Trindade, Y.T., Rodrigues, E.A., Dias-da-Costa, D., 2018. Modeling reinforced concrete structures using coupling finite elements for discrete representation of reinforcements. Finite Elem. Anal. Des. 149, 32–44. http://www.sciencedirect.com/science/article/pii/S0168874X18301082.

Caggiano, A., Etse, G., Martinelli, E., 2012. Zero-thickness interface model formulation for failure behavior of fiber-reinforced cementitious composites. Comput. Struct. 98–99, 23–32. http://www.sciencedirect.com/science/article/pii/S0045794912000284.

Carol, I., Prat, P., López, C., 1997. Normal/shear cracking model: application to discrete crack analysis. J. Eng. Mech. 123 (8), 765–773. https://doi.org/10.1061/(ASCE)0733-9399(1997)123:8(765).

Cervera, M., Oliver, J., Manzoli, O., 1996. A rate-dependent isotropic damage model for the seismic analysis of concrete dams. Earthquake Eng. Struct. Dyn. 25 (9), 987–1010.

Cunha, V., 2010. Steel fibre reinforced self-compacting concrete – from micromechanics to composite behaviour Ph.D. thesis. Department of Civil Engineering, University of Minho, Portugal.

Cunha, V., Barros, J., Sena-Cruz, J., 2011. An integrated approach for modelling the tensile behaviour of steel fibre reinforced self-compacting concrete. Cem. Concr. Res. 41 (1), 64–76. http://www.sciencedirect.com/science/article/pii/S0008884610002115.

Cunha, V., Barros, J., Sena-Cruz, J., 2012. A finite element model with discrete embedded elements for fibre reinforced composites. Comput. Struct. 94 - 95 (0), 22–33. http://www.sciencedirect.com/science/article/pii/S0045794911003038.

Deluce, J.R., 2011. Cracking Behaviour of Steel Fibre Reinforced Concrete Containing Conventional Steel Reinforcement. University of Toronto, Toronto, ON, Canada Master's thesis.

EN 14651, 2007. Test method for metallic fiber concrete – measuring the flexural tensile strength (limit of proportionality (LOP), residual). European Committee Stardardization.

Etse, G., Caggiano, A., Vrech, S., 2012. Multiscale failure analysis of fiber reinforced concrete based on a discrete crack model. Int. J. Fract. 178 (1–2), 131–146. https://doi.org/10.1007/s10704-012-9733-z.

Fang, Q., Zhang, J., 2013. Three-dimensional modelling of steel fiber reinforced concrete material under intense dynamic loading. Constr. Build. Mater. 44, 118–132. http://www.sciencedirect.com/science/article/pii/S0950061813001967.

Hartig, J., Häußler-Combe, U., Schicktanz, K., 2008. Influence of bond properties on the tensile behaviour of textile reinforced concrete. Cem. Concr. Compos. 30 (10), 898–906. http://www.sciencedirect.com/science/article/pii/S0958946508001121.

Kang, J., Bolander, J.E., 2015. Multiscale modeling of strain-hardening cementitious composites. Mech. Res. Commun.

Kang, J., Kim, K., Lim, Y.M., Bolander, J.E., 2014. Modeling of fiber-reinforced cement composites: discrete representation of fiber pullout. Int J Solids Struct 51 (10), 1970–1979. http://www.sciencedirect.com/science/article/pii/S0020768314000547.

Laranjeira, F., 2010. Design-oriented constitutive model for steel fiber reinforced concrete Ph.D. thesis. Universidad Politécnica de Cataluña, Barcelona - Spain.

Laranjeira, F., Aguado, A., Molins, C., 2010a. Predicting the pullout response of inclined straight steel fibers. Mater. Struct. 43 (6), 875–895. https://doi.org/10.1617/s11527-009-9553-4.

Laranjeira, F., Molins, C., Aguado, A., 2010b. Predicting the pullout response of inclined hooked steel fibers. Cem. Concr. Res. 40 (10), 1471–1487. http://www.sciencedirect.com/science/article/pii/S0008884610001249.

Lee, D.H., Hwang, J.-H., Ju, H., Kim, K.S., Kuchma, D.A., 2012. Nonlinear finite element analysis of steel fiber-reinforced concrete members using direct tension force transfer model. Finite Elem. Anal. Des. 50 (0), 266–286. http://www.sciencedirect.com/science/article/pii/S0168874X11002022.

Lee, S.-C., Cho, J.-Y., Vecchio, F., 2011. Diverse embedment model for steel fiber-reinforced concrete in tension: model development. ACI Mater. J. 108 (5), 516–525.

Manzoli, O., Gamino, A., Rodrigues, E., Claro, G., 2012. Modeling of interfaces in two-dimensional problems using solid finite elements with high aspect ratio. Comput. Struct. 94–95 (0), 70–82. http://www.sciencedirect.com/science/article/pii/S0045794911002938.

Manzoli, O.L., Oliver, J., Huespe, A., Diaz, G., 2008. A mixture theory based method for three-dimensional modeling of reinforced concrete members with embedded crack finite elements. Comput. Concrete 5 (6), 401–416.

Mora, D., Oliver, J., A.E., H., 2011. Computational modeling of fiber reinforced cement composites as a complex material. Congress on Numerical Methods in Engineering 2011.

Oliver, J., Huespe, A., Blanco, S., Linero, D., 2006. Stability and robustness issues in numerical modeling of material failure with the strong discontinuity approach. Comput. Methods Appl. Mech. Eng. 195 (52), 7093–7114. Computational Modelling of Concrete, http://www.sciencedirect.com/science/article/pii/S0045782505003920.

Oliver, J., Huespe, A., Cante, J., 2008. An implicit/explicit integration scheme to increase computability of non-linear material and contact/friction problems. Comput. Methods Appl. Mech. Eng. 197 (21–24), 1865–1889. http://www.sciencedirect.com/science/article/pii/S0045782507004756.

Parés, A.P., 2011. Numerical Approach for Modeling Steel Fiber Reinforced Concrete Ph.D. thesis. Universidad Politécnica de Cataluña, Barcelona - Spain.

Peerlings, R.H.J., de Borst, R., Brekelmans, W.A.M., de Vree, J.H.P., 1996. Gradient enhanced damage for quasi-brittle materials. Int. J. Numer. Methods Eng. 39 (19), 3391–3403.

Prazeres, P.G.C., Bitencourt Jr., L.A.G., Bittencourt, T.N., Manzoli, O.L., 2015. A modified implicit-explicit integration scheme: an application to elastoplasticity problems. J. Brazilian Soc. Mech. Sci. Eng. 1–11. https://doi.org/10.1007/s40430-015-0343-3.

Pros, A., Diez, P., Molins, C., 2012. Modeling steel fiber reinforced concrete: numerical immersed boundary approach and a phenomenological mesomodel for concrete-fiber interaction. Int. J. Numer. Methods Eng. 90 (1), 65–86. https://doi.org/10.1002/nme.3312.

Radtke, F., Simone, A., Sluys, L., 2010. A computational model for failure analysis of fibre reinforced concrete with discrete treatment of fibres. Eng. Fract. Mech. 77 (4), 597–620. http://www.sciencedirect.com/science/article/pii/S0013794409003555.

Radtke, F.K.F., Simone, A., Sluys, L.J., 2011. A partition of unity finite element method for simulating non-linear debonding and matrix failure in thin fibre composites. Int. J. Numer. Methods Eng. 86 (4–5), 453–476. https://doi.org/10.1002/nme.3056.

Rolf, B., Günther, M., Fanbing, S., Yijian, Z., 2013. Experimental, analytical and numerical analysis of the pullout behaviour of steel fibres considering different fibre types, inclinations and concrete strengths. Structural Concrete 15 (2), 126–135. https://onlinelibrary.wiley.com/doi/abs/10.1002/suco.201300058.

S.K., P., Ramaswamy, A., 2002. A finite element assessment of flexural strength of prestressed concrete beams with fiber reinforcement. Cement Concrete Compos. 24, 229–241.

Soroushian, P., Lee, C.-D., 1990. Distribution and orientation of fibers in steel fiber reinforced concrete. ACI Mater. J. 87 (5), 433–439.

Voo, J.Y.L., Foster, S.J., 2003. Variable Engagement Model for Fibre Reinforced Concrete in Tension. Technical Report, R-420. School of Civil and Environmental Engineering, The Universiity of New South Wales, Sydney, Australia.

Vrech, S., Etse, G., Caggiano, A., 2016. Thermodynamically consistent elasto-plastic microplane formulation for fiber reinforced concrete. Int. J. Solids Struct. 81, 337–349. http://www.sciencedirect.com/science/article/pii/S0020768315004990.

Švec, O., Žirgulis, G., Bolander, J.E., Stang, H., 2014. Influence of formwork surface on the orientation of steel fibres within self-compacting concrete and on the mechanical properties of cast structural elements. Cem. Concr. Compos. 50, 60–72. http://www.sciencedirect.com/science/article/pii/S0958946513002011.

Zhan, Y., Meschke, G., 2014. Analytical model for the pullout behavior of straight and hooked-end steel fibers. J. Eng. Mech. 140 (12), 04014091.

Zhan, Y., Meschke, G., 2016. Multilevel computational model for failure analysis of steel-fiber-reinforced concrete structures. J. Eng. Mech. 142 (11), 04016090.